Nickel–Sulfonate Mode of Substrate Binding for Forward and Reverse Reactions of Methyl-SCoM Reductase Suggest a Radical Mechanism Involving Long-Range Electron Transfer

Anjali Patwardhan, Ritimukta Sarangi, Bojana Ginovska, Simone Raugei, and Stephen W. Ragsdale*

ABSTRACT: Methyl-coenzyme M reductase (MCR) catalyzes both the synthesis and the anaerobic oxidation of methane (AOM). Its catalytic site contains Ni at the core of cofactor F_{430}. The Ni ion, in its low-valent Ni(I) state, lights the fuse leading to homolysis of the C–S bond of methyl-coenzyme M (methyl-SCoM) to generate a methyl radical, which abstracts a hydrogen atom from coenzyme B (HSCoB) to generate methane and the mixed disulfide CoMSSCoB. Direct reversal of this reaction activates methane to initiate anaerobic methane oxidation. On the basis of the crystal structures, which reveal a Ni–thiol interaction between Ni(II)–MCR and inhibitor CoMSH, a Ni(I)–thioether complex with substrate methyl-SCoM has been transposed to canonical MCR mechanisms. Similarly, a Ni(I)–disulfide with CoMSSCoB is proposed for the reverse reaction. However, this Ni(I)–sulfur interaction poses a conundrum for the proposed hydrogen-atom abstraction reaction because the >6 Å distance between the thiol group of SCoB and the thiol of SCoM observed in the structures appears to be too long for such a reaction. The spectroscopic, kinetic, structural, and computational studies described here establish that both methyl-SCoM and CoMSSCoB bind to the active Ni(I) state of MCR through their sulfonate groups, forming a hexacoordinate Ni(I)–N/O complex, not Ni(I)–S. These studies rule out direct Ni(I)–sulfur interactions in both substrate-bound states. As a solution to the mechanistic conundrum, we propose that both the forward and the reverse MCR reactions emanate through long-range electron transfer from the Ni(I)–sulfonate complexes with methyl-SCoM and CoMSSCoB, respectively.

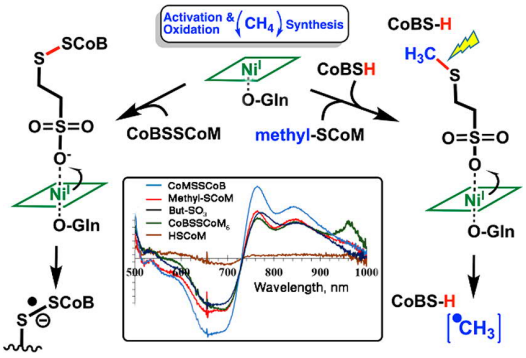

INTRODUCTION

Methyl-coenzyme M reductase (MCR), one of the few Ni proteins in nature, catalyzes the reaction of methyl-coenzyme M (CH_3–SCoM) with coenzyme B (HSCoB) in methanogenic archaea to form methane and the heterodisulfide CoMSSCoB (eq 1).[1] MCR also catalyzes the reverse reaction in consortia of anaerobic methane oxidizing archaea (ANME) with sulfate, nitrate, or Fe(III)-reducing bacteria.[2] This study describes the relative orientations of the substrates in the forward and reverse reactions of MCR. Spectroscopic, structural, and computational studies identify an unexpected and symmetric complex between active Ni(I) enzyme and the sulfonate group of the substrates for the forward and reverse reactions of eq 1. These results suggest the need to reassess how catalysis is triggered in the MCR mechanism.

$$CH_3\text{-SCoM} + \text{HSCoB} \rightarrow CH_4 + \text{CoMSSCoB}$$
$$\Delta G^0 \approx -30\ \text{kJ/mol} \quad (1)$$

Understanding the biosynthesis of methane is important from basic energy, economic, and environmental perspectives. Methane accounts for 22% of U.S. energy consumption,[3,4] with one-half of homes using natural gas as their heating fuel. Methane is the simplest organic compound, but it has the highest energy content of any carbon-based fuel. About 90–95% of all methane on earth is produced biogenically.[5] Methanogens, responsible for enzymatic synthesis of 1 billion tons of methane per year,[6] are its major source, the balance generated by metabolism of methyl–mercury[7] and methylphosphonate.[8] Much of the methane formed by methanogens is captured and used as an energy source by aerobic and anaerobic methanotrophic (ANME) microbes.[9,10] However, the increased mining of methane and industrial farming of cattle and other ruminants since the industrial revolution has created a mismatch between the sources and the sinks of methane, causing its atmospheric levels to double over the past two centuries.[11] This is an environmental concern related to climate change because pound for pound, methane causes 25 times more global warming

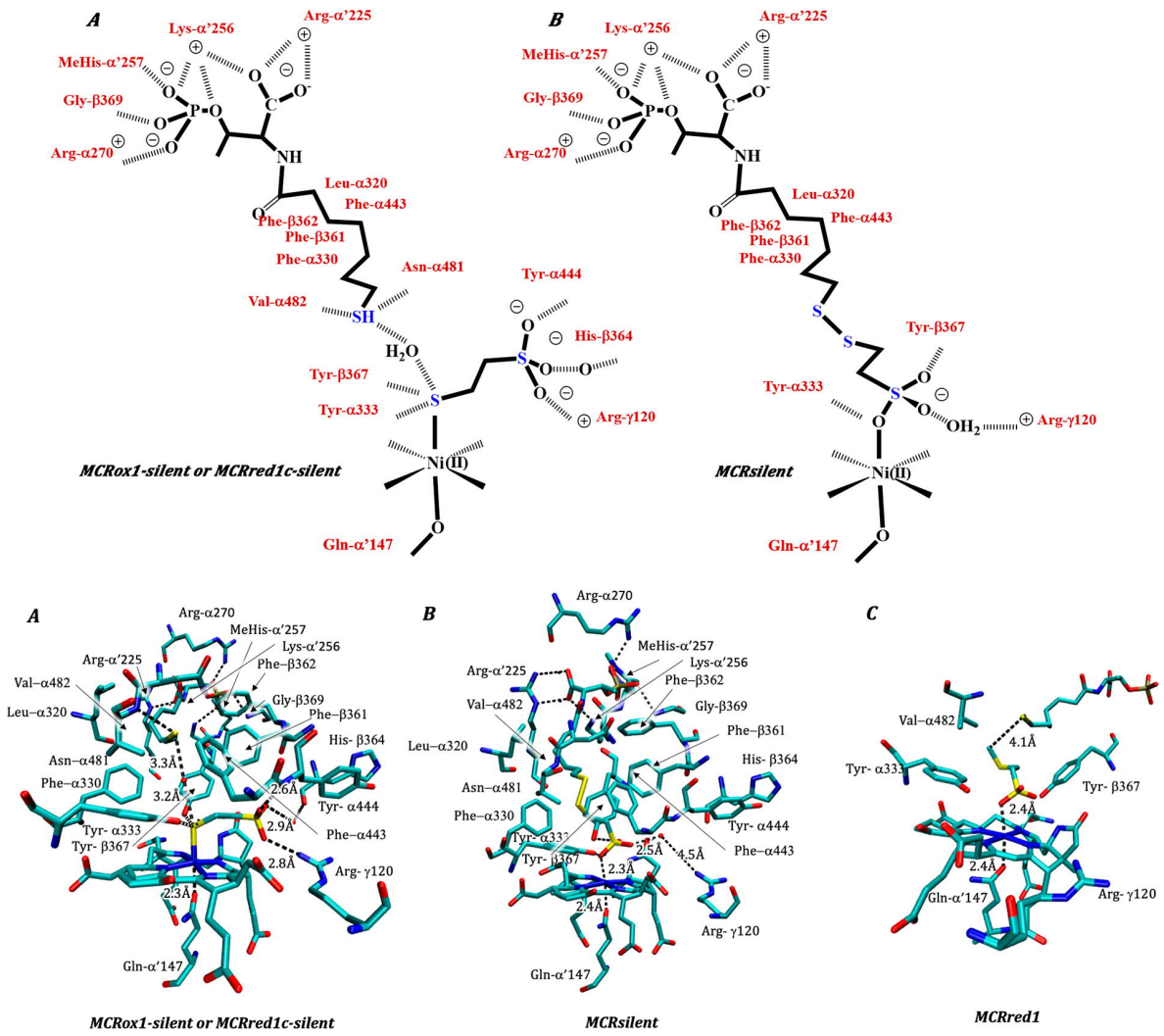

Figure 1. Representative interactions in the active site of MCR. (Top and bottom A) MCRox1-silent or MCRred1c-silent with CoMSH bound to Ni(II). (Top and bottom B) MCR-silent with CoMSSCoB bound to Ni(II). Structure details obtained from pdb 1mro. (Bottom C) Ni(I)−MCRred1 with methyl-SCoM and HSCoB modeled into the active site showing the predicted distances between the *S*-methyl carbon and the HSCoB hydrogen atom to undergo abstraction. (C) F_{430} and all residues except for methyl-SCoM and the HS-CH_2−CH_2− tail of HSCoB are from pdb 1hbm. Calculated QM model (Figure 5, model 3) was overlapped with pdb 1hbm based on the subset of atoms fixed in the crystal structure position during the optimization, and all atoms except for those representing the substrates were removed.

over a 100 year period than CO_2, the other major greenhouse gas.[12]

Besides the importance of methane metabolism in our environment and global energy landscape, the basic chemistry and biology of alkane activation and formation by MCR are intriguing. Because of methane's strong sp^3 C−H bonds, low solubility in both polar and nonpolar solvents, and very high ionization energy, selective activation and functionalization of the C−H bond of methane was dubbed one of the holy grail reactions in chemistry.[13] MCR accomplishes this reaction, as well as methane synthesis, using a reduced Ni−hydrocorphin cofactor F_{430}[14−17] related to porphyrin, chlorophyll, and vitamin B_{12} along with second-sphere amino acid residues as catalysts. Computational[18] and experimental[19] results indicate that methane formation and oxidation by MCR occur through a mechanism involving methyl, thiyl, and disulfide anion radicals.[20]

A variety of crystal structures of MCR in the presence (and absence) of substrates have been published.[21−25] It is a multimeric enzyme composed of three subunits MCRA (α), MCRB (β), and MCRG (γ) in an $\alpha_2\beta_2\gamma_2$ conformation with a reduced hydrocorphin Ni cofactor F_{430} buried at the end of a 30 Å long substrate channel. The F_{430} is anchored via a combination of electrostatic and H-bond interactions between the carboxylate side chains and the protein backbone (Figure 1). A weak distal Ni−O bond (O-α'Gln) is present in all forms of the Ni(II) enzyme as well as the Ni(I) states, MCRred1, MCRred1-silent, and Ni(III)-MCR-Me.[21,26] The coordination environment of the different states of MCR is shown in Figure 2. As discussed by Thauer,[20] the oxidation state of MCRox1 has been formulated as Ni(I) and Ni(III) and is now generally accepted to resonate between a Ni(III)−thiolate and a Ni(II)−thiyl radical. The lower axial Gln residue moves in (2.1 Å, 6 coordinate) or away (2.3 Å, 5 coordinate) from the Ni based on the presence or absence of the upper axial ligand and may play a role in fine tuning the redox potential of the Ni center and/or provide stability during catalysis.[21] Two moles of F_{430} bind the hexameric protein at identical but distinct substrate binding

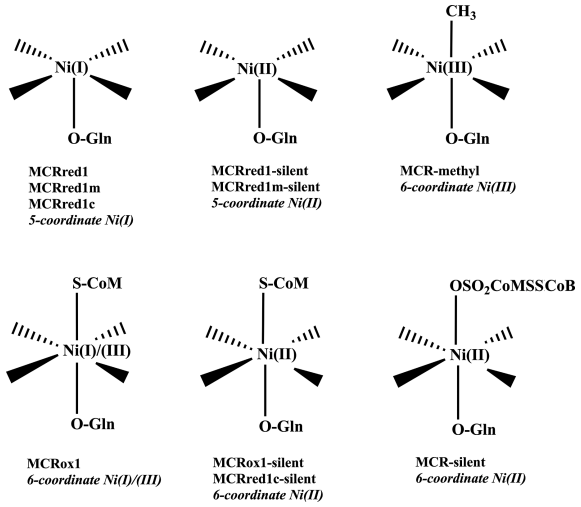

Figure 2. Various states of MCR with their observed oxidation states and coordination geometries. Ni(I) states include methyl-SCoM-bound MCRred1m and MCRred1 and CoM-bound MCRred1c. MCRox1state contains Ni(I) or Ni(III) (see text). Corresponding Ni(II) states include MCRred1-silent, MCRred1m-silent, MCRred1c-silent, and MCRox1-silent and CoMSSCoB-bound MCR-silent.

sites separated by 50 Å. The catalytic Ni site is accessible only through this channel and only to small molecules up to a diameter of 6 Å.[21]

Regarding binding of CoM, the crystal structures of the Ni(II)−MCRred1-silent and MCRox1-silent states show its thiolate anchored by binding axially to the Ni(II) on one side and its negatively charged sulfonate group forming a salt bridge to the guanidinium group of Arg-γ120 (Figure 1).[21,27] XAS results similarly indicate S coordination to the Ni in the MCRox1 and MCRox1-silent states, while the MCR-silent state (with CoMSSCoB bound) fits best with 4N ligands and 2N/O ligands in the axial position to give a hexacoordinate Ni center (Figure 2).[26,28] Ni K pre-edge and EXAFS data and time-dependent DFT (TD-DFT) calculations also reveal an axial Ni−S bond from the thiolate of CoMSH in the Ni(II)−MCRred1-silent and MCRox1-silent states.[29] This Ni−thiolate appears to interact with a water molecule that bridges CoMSH and HSCoB in addition to forming hydrogen bonds to the hydroxyl groups of Tyr-α333 and Tyr-β367[27] (Figure 1). On the other hand, Grabarse et al.[27] speculate that the hydrophobicity of the pocket would exclude a solvent molecule and that this density between CoMS−Ni(II) and HSCoB arises from a methyl radical generated during X-ray exposure of the crystal.

HSCoB hangs down the substrate binding channel tethered by electrostatic interactions between its negatively charged threonine phosphate moiety and five positively charged amino acids. Its heptanoyl [$(CH_2)_6$−CO−] arm stretches over 16 Å in van der Waals contact with several hydrophobic residues, namely, Phe-α330, Tyr-α333, Phe-α443, Phe-β361, and Tyr-β367 positioned along the substrate binding pocket (Figure 1). At its end, the HSCoB thiol group is 8.8 Å from the Ni center and interacts with the side chain nitrogen of Asn-α481, the main chain peptide nitrogen of Val-α482, and a bridging water molecule. Asn-α481 is within hydrogen-bonding distance of the sulfur in the post-translationally modified thioglycine (TGly)-α445.[21]

Crystal structures show that various $HSCoB_{5-9}$ analogs are anchored at an annulus of charged residues at the top of the

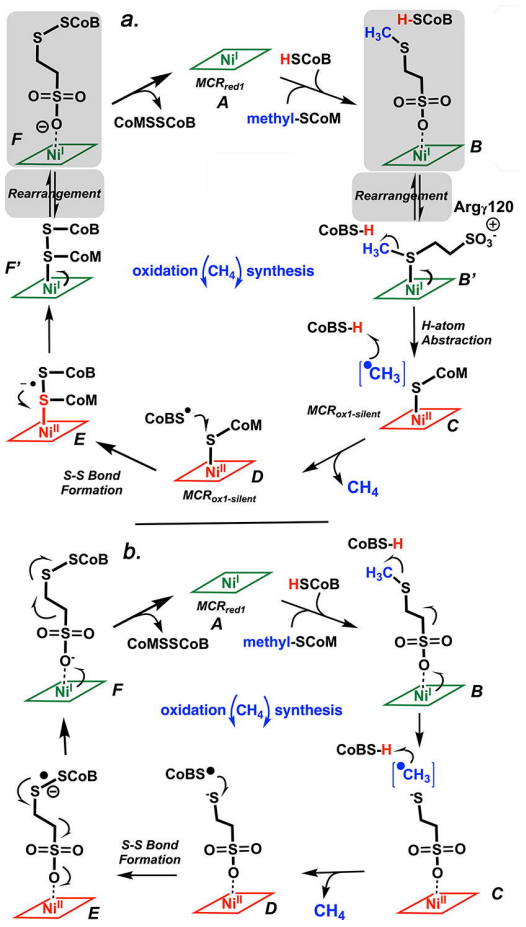

Figure 3. Contrasting mechanisms of activation of methane synthesis. (Top, a) Canonical mechanism through Ni(I)−S species with direct Ni → sulfur ET. Shaded portion includes the sulfonate-bound substrates, which could rearrange to form Ni−thiol (B′ or F′) states proposed to be the productive state in the canonical mechanism. (Bottom, b) Proposed mechanism of CH_4 synthesis involving Ni−sulfonate species (B) as productive complexes and long-distance ET.

substrate channel and adopt similar positions as they thread into the channel toward the Ni-cofactor.[25] The thiol group of the slow substrate $HSCoB_6$ situates at the same position as that of the native substrate, i.e., 8.8 Å from the Ni, leaving a 6.4 Å gap between the thiol group of HSCoB/$HSCoB_6$ and the Ni-bound S of CoM. Since a methyl group of CH_3−SCoM cannot bridge this large gap,[30] a conformational change was proposed to allow HSCoB to penetrate deeper into the substrate channel toward the Ni ion. The $HSCoB_5$ thiol group rests 9.3 Å from the Ni as would be expected, while the SH groups of $HSCoB_8$/$HSCoB_9$ are located 5.9−6.2 Å from the Ni of F_{430}. The crystal structures of MCR with the HSCoBx analogs did not reveal any of the conformational changes proposed to occur during catalysis, suggesting a more important role for methyl-SCoM, CoMSH, and the oxidation states of the Ni−F_{430} in the catalytic cycle[25] (Figure 2). Furthermore, the structure of MCR-CoMSSCoB (MCR-silent) reveals the HSCoB portion in virtually the same place as in MCRox1-silent.[27,31] Thus, the large distance in these structures[25,27,31] between the HSCoB hydrogen atom to be abstracted and the methyl group, which is proposed to undergo homolytic fission promoted by a Ni(I)−SCoM interaction,

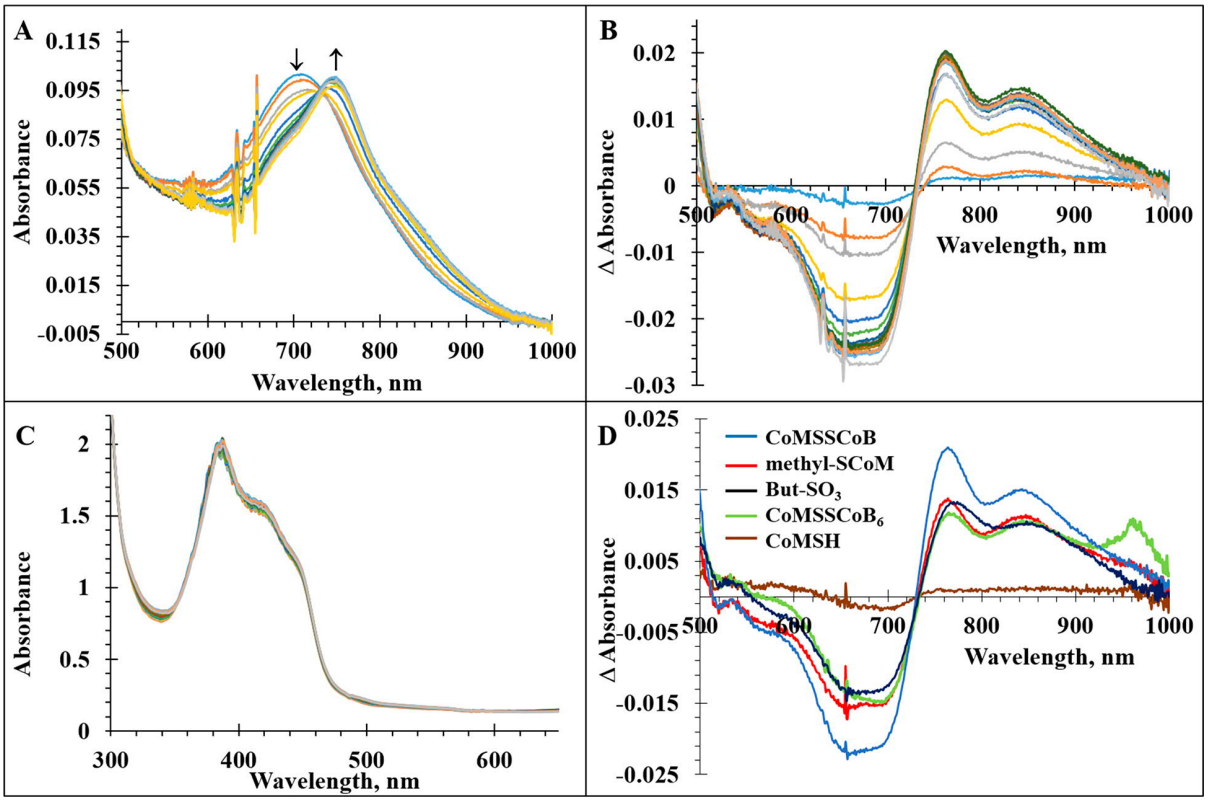

Figure 4. Binding of substrates monitored by NIR spectroscopy. (A) Red shift in λ_{max} from 700 to 750 nm of Ni(I)−MCRred1 (50 μM) with increasing concentration of CoMSSCoB (0−700 μM). (B) Difference spectra of the spectra in A, highlighting the buried peaks at 768 and 850 nm on CoMSSCoB addition. (C) Absorbance at 385 nm(Ni(I)) and 420 nm (Ni(II)) remains unchanged during addition of the substrate, suggesting no redox reaction at the Ni(I) center. (D) Comparative difference spectra for addition of 500 μM each of CoMSH (brown), methyl-SCoM (red), CoMSSCoB (blue), CoMSSCoB$_6$ (green), and But-SO$_3$ (black) to MCRred1 (50 μM).

poses a conundrum for all published MCR catalytic mechanisms, as highlighted in Figure 3a.

One significant issue is that all published crystal structures are of inactive Ni(II) or a methyl−Ni(III) state—none are available for the active Ni(I) state. In our studies of the binding of HSCoB analogs,[25] although the crystallizations were set up and mounted with MCR in the Ni(I)−MCRred1 state, by the time X-ray diffraction data were collected they had undergone oxidation to the Ni(II)−MCRred1-silent state, as assessed by single-crystal UV−vis microspectrophotometry; furthermore, following data collection, there was no evidence for photoreduction of the Ni(II) back to Ni(I) in any of the crystals. Attempts to photoreduce the crystals using different wavelengths and temperatures were also unsuccessful.

Thus, spectroscopic studies are crucial to obtaining an accurate description of the coordination chemistry of the Ni(I) state. In this respect, X-ray absorption spectroscopy (XAS) is highly significant because it provides extremely precise measurement of the Ni oxidation state and metal−ligand bond distances as well as discrimination between the thiolate and the nitrogen or oxygen ligation. Furthermore, these experiments can be carried out under strictly anaerobic conditions. Similarly, electron paramagnetic resonance (EPR)-based studies provide an independent view of the d^9 Ni(I) state. For example, on the basis of EPR, electron nuclear double resonance (ENDOR), and quantum mechanical calculations, Hinderberger et al. proposed that the thioether−S of methyl-SCoM and one of the H atoms of the methyl group are between 3.45 and 3.75 Å and 5.35 and 5.65 Å, respectively, from the Ni center.[32] This binding mode does not bring the thioether−S within bonding distance of the Ni.

In this contribution, we describe near-infrared (NIR), XAS, and EPR results to characterize the active Ni(I) state of MCR. The pK_a values measured using acid−base titrations and ^{1}H and ^{31}P NMR are utilized to determine the ionization states of the substrates for the molecular models used in the computational studies. QM-MM and TD-DFT studies on these chemical models successfully describe the binding details. The spectroscopic, kinetic, structural, and computational studies described here establish that methyl-SCoM binds to the active Ni(I) state of MCR through its sulfonate, forming a hexacoordinate Ni(I) complex. This is unusual; most Ni(I) complexes are four or five coordinate.[33] We are aware of only one other structurally characterized six-coordinate model Ni(I) complex.[34] Here, we also suggest a solution to the apparent conundrum of how the methyl radical can attack the H of HSCoB. As shown in Figure 3b, we propose a revised mechanism for MCR catalysis in which methyl-SCoM binds to Ni(I) through its sulfonate group. We suggest that this is the state from which catalysis ensues.

RESULTS

Changes in Near-Infrared Bands on Addition of Substrates: Comparison among the Various Substrates. In the UV−vis region, Ni(I) has a characteristic absorbance at 385 nm which changes to 420 or 445(sh) nm on oxidation to Ni(II) or Ni(III). Ni(I)−MCRred1 also exhibits the characteristic d−d transition in the near-infrared (NIR) region of the

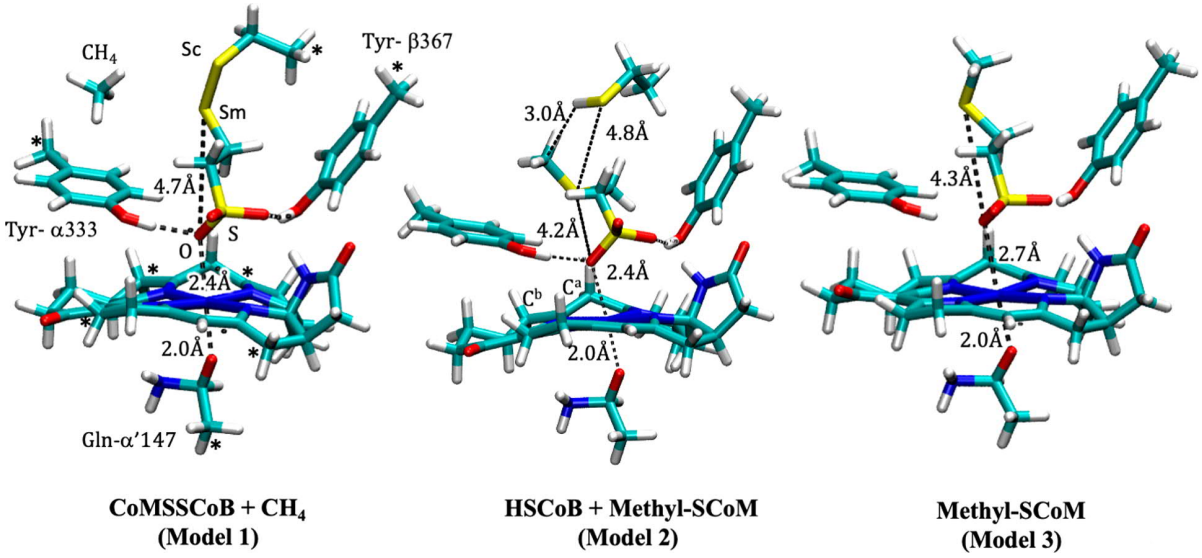

Figure 5. Structures optimized using DFT: (1) Ni(I) binding CoMS-SCoB, where HSCoB is truncated after the second carbon from the S_c, (2) Ni(I) binding HSCoB and methyl-SCoM, and (3) Ni(I) binding methyl-SCoM. All models were built starting from crystal structure 1hbm. Truncation points from the enzyme are annotated with asterisks and were fixed in place during optimization.

electromagnetic spectrum that is absent in Ni(II) states like MCRred1-silent. Addition of substrates CoMSSCoB and methyl-SCoM to 50 μM Ni(I)−MCRred1 (between 65% and 70% Ni(I) for various purifications) elicits significant changes in these NIR bands over a time frame that the 385 nm UV−vis band associated with Ni(I) does not change. Thus, we attribute these changes to shifts in the d−d orbital energies of Ni(I) that can be monitored to elucidate the nature of substrate binding.

Addition of HSCoB does not elicit NIR changes. However, titration of Ni(I)−MCRred1 (50 μM) with the first substrate in the reverse reaction, CoMSSCoB or $CoMSSCoB_6$ (0−500 μM), shifts the broad 700 nm peak to ∼750 nm (Figure 4A). The breadth of these d−d transitions makes it difficult to precisely monitor the wavelength maxima due to overlap. We employed difference spectra to more accurately quantify these changes at the exact wavelengths. Difference spectra (Figure 4B) show that the decrease in absorbance at 700 nm is associated with an increase at 768 and 850 nm for both substrates. The absorbance at 385 nm characteristic of Ni(I) in MCRred1 remains unchanged as the NIR spectra shift, demonstrating that the decrease in absorbance at 700 nm is due to binding and not due to oxidation of Ni(I) (Figure 4C) associated with catalysis. Oxidation of Ni(I) to Ni(II) occurs over a longer time frame associated with decay of the NIR bands as the 385 nm band shifts to 420 nm (Figure S5). Thus, these NIR changes can confidently be assigned to d−d changes associated with substrate binding alone.

Addition of methyl-SCoM and even butanesulfonate (But-SO_3) to MCRred1 gives rise to the same NIR spectral changes (Figure 4D), while the 385 nm Ni(I) absorbance remains unchanged. These changes in d−d transitions suggest that CoMSSCoB, $CoMSSCoB_6$, But-SO_3, and methyl-SCoM all bind to Ni(I) in a similar fashion within the enzyme pocket. But-SO_3 lacks the S proposed as the Ni ligand in the canonical mechanism, strongly indicating the formation of a Ni(I)−sulfonate bond in all of these substrates and analogs.

On the other hand, addition of CoMSH does not result in any shifts in the NIR or, as discussed below, EPR spectra (Figure 12A). Furthermore, previous XAS studies have shown that the Ni(I) in MCRred1 remains 5 coordinate in the presence of CoMSH.[26] Thus, the lack of NIR changes upon addition of CoMSH indicates that, unlike the Ni(II) state, five-coordinate Ni(I)−MCRred1 does not form a Ni(I)−thiolate complex with CoMSH. On the other hand, addition of HSCoB to MCRred1 bound to CoMSH does appear to bring the S− of CoMSH closer to the Ni(I),[20] a phenomenon that requires further study.

Our interpretation of these substrate-induced spectral changes is that addition of HSCoB alone or CoMSH does not result in any change in the Ni(I) d−d bands, suggesting that these substrates do not alter the five-coordinate Ni(I) state. On the other hand, addition of methyl-SCoM or either of the heterodisulfide substrates results in formation of a similar six-coordinate Ni(I) state. These conclusions are validated by XAS and computational results, as described below.

Quantum chemical truncated models (Figure 5) of the MCR active site containing Ni(I) binding either CoMSSCoB (model 1) or methyl-SCoM (the latter with or without HSCoB, model 2 or 3, respectively) were investigated to elucidate the Ni−sulfonate interaction and its effect on the NIR spectra. In Figure 5 and Table 1, Sm and Sc designate the S atoms on HSCoB (Sc) and CoMSH (Sm). On the basis of the pK_a measurements reported below, the sulfonate groups of methyl-SCoM and CoMSSCoB were modeled as deprotonated. Because all models

Table 1. Characteristic Bond Distances for the Crystal Structure and the Three Models in Figure 5 Calculated Using a Gas-Phase DFT Approach

bond distance (Å)	1hbm	CoMSSCoB + CH_4	HSCoB + methyl-SCoM	methyl-SCoM
Ni−O(Gln147)	2.35	2.03	2.03	2.04
Ni−O(SO_3^-)	2.29	2.41	2.41	2.71
Ni−S(SO_3^-)	3.29	3.42	3.45	3.62
Ni−S_m[a]	6.71	7.04	6.09	6.98
Ni−S_c[b]	8.46	8.47	8.48	n/a
C(Me)−S_c	n/a	4.41	3.72	n/a

[a]S_m = sulfur atom of the CoM moiety of methyl-SCoM. [b]S_c = sulfur atom of the HSCoB moiety.

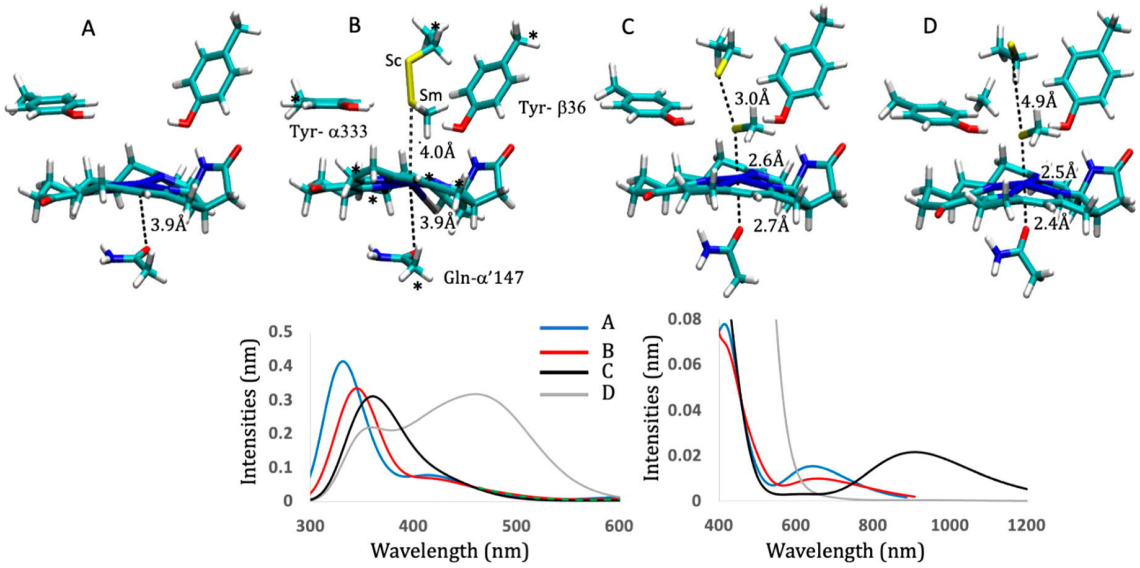

Figure 6. Computational models of the canonical mechanism involving Ni−S_m coordination and TD-DFT calculations of MCR UV−vis and NIR spectra (**B**) and bond formation (**C** and **D**). All models were previously reported.[35] Structures **A** and **B** are of the Ni(I) state, and **C** and **D** are Ni(II). (a) Major features of the spectra as captured by the TD-DFT calculations for all models shown on the bottom panels and are able to qualitatively capture the shifts in the various structures (bottom, left). (b) d−d transitions are captured for structures **A** (MCRred1) and **B** (MCRred1 + CoMSSCoB) at ∼650 nm (bottom, right).

truncated HSCoB at the second carbon, protonation of the phosphate group does not affect these calculations. The geometries of the optimized structural models are reported in Figure 5 along with relevant geometrical parameters. Additional geometrical parameters are summarized and compared with those from the 1.8 Å resolution crystal structure of the MCR product complex (pdb entry1hbm) in Table 1. All models show stable complexes of Ni with the SO_3^- group and Gln147 residue via oxygen as well as the interaction of the substrate with the OH groups of the Tyr residues.

The spectra of the previous structural models for a Ni−S_m coordination (Figure 6, models **A**−**D**) and for structural models (Figure 7) for Ni coordination with SO_3^- of methyl-SCoM considered in the present work were simulated in a time-dependent DFT (TD-DFT) framework. Figures 6 and 7 show that the adopted computational setup captures well the major spectral features and, importantly, qualitatively captures the shifts in the various structures. For structures **A** and **B** in Figure 6, which are Ni(I), the characteristic peak is calculated to be around ∼340 nm. As the S−S bond is broken, the S_m−Ni bond is formed (structures **C** and **D**) and Ni center changes from Ni(I) to Ni(II) as the peak shifts toward ∼460 nm, in agreement with the experimentally observed shifts. In particular, the d−d transitions for structures **A** and **B** are captured at ∼650 nm (Figure 6b). For the structures with Ni−O coordination (Figure 7 and 8), the d−d transitions in the NIR spectrum are slightly shifted to ∼600 nm with some low-intensity d−d transitions found beyond 780 nm. These calculations suggest that the spectral features observed experimentally can be assigned to the structures exhibiting Ni−SO_3^- interactions. No CT transitions were found in the calculated spectral region with any of the systems.

Binding Constants for Methyl-SCoM, CoMSSCoB, and CoMSSCoB$_6$. A plot of the NIR changes shows that the decrease in absorbance at 700 nm matches the concomitant increase at 768 and 850 nm for CoMSSCoB, CoMSSCoB$_6$, and methyl-SCoM (Figure 9A) The data are fit to a one-site binding

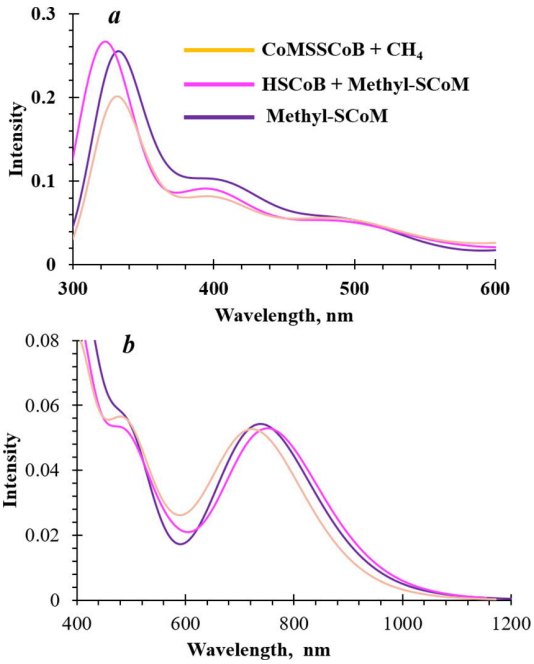

Figure 7. TD-DFT calculations of MCR UV−vis and NIR spectra. (a) Major features of the spectra as captured by the TD-DFT calculations for the models shown in Figure 5 qualitatively capture the shifts in the various structures. (b) Spectral region from 600 to >800 nm captures d−d transitions for all three structures. More prominent peak at ∼740 nm is due to a F_{430} π to π^* transition, which overlaps some of the captured d−d transitions.

isotherm, where the fraction of bound enzyme is plotted versus the concentration of the substrate. For the reverse reaction substrates, the K_d values are 57.4 ± 5.4 μM for CoMSSCoB and 105.3 ± 10.9 μM for CoMSSCoB$_6$ (Figure 9B). The K_d for methyl-SCoM is 27.5 ± 7.3 μM (Figure 9C), which is similar to

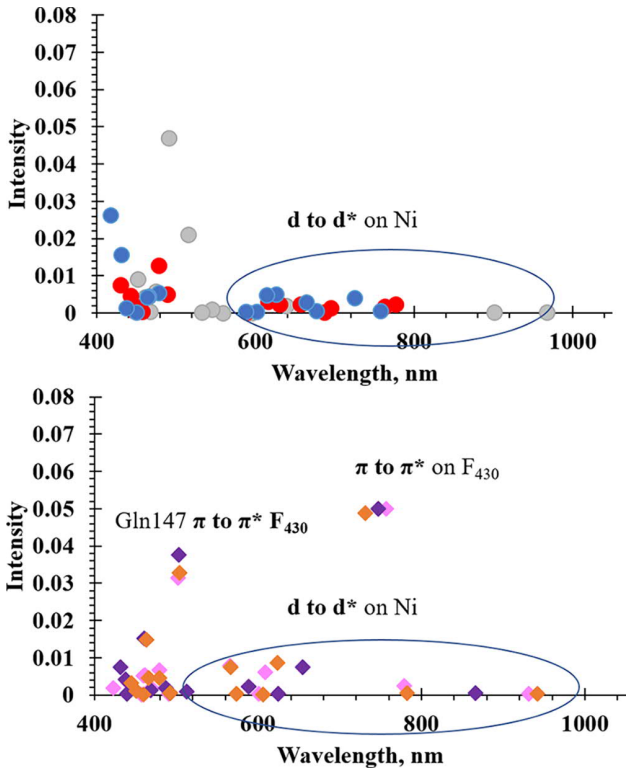

Figure 8. Excitation from TD-DFT used in reconstructing the spectra. Calculated transitions used to reproduce the spectra in the d−d region for all models shown in Figures 5 (top) and 6 (bottom).

the value (13 ± 4 μM) obtained by fluorescence spectroscopy.[36] The tighter binding for methyl-SCoM is as expected, since MCR relies on the strict binding order of substrates to initiate catalysis. The K_d values for the heterodisulfide substrates are similar to that for HSCoB (90 ± 22 μM) as measured by fluorimetry,[36] presumably dictated by the strong electrostatic interactions at the top of the channel between the positively charged protein residues (Figure 1) and the carboxylate and phosphate groups of the CoB moiety.

The only structural feature in common among methyl-SCoM and the heterodisulfide substrates relevant to Ni coordination is their sulfonate group (although the sulfurs are similar, thioether and disulfide), indicating formation of the upper axial Ni−O (sulfonate) ligand with these three substrates. Thus, we studied MCR binding to butanesulfonate, which maintains the carbon chain and the sulfonate group but lacks the −S atom that all canonical mechanisms (as shown in Figure 3a) postulate to bind to the Ni(I) during the first step of catalysis of both the forward and the reverse methane synthesis reactions. Upon addition of butanesulfonate, the same NIR spectral shifts are observed as with the other substrates but with a much higher K_d value of 3.3 ± 0.6 mM (Figure 9D). This high value of K_d can be due to the lack of the S, which is stabilized via hydrogen-bond interactions with the Tyr-333 residue in the catalytic pocket.

Measurement of pK_a Values for the Sulfonate, Carboxylate, Phosphate, and Thiol Groups by Acid−Base Titrations and ^{31}P and ^{1}H NMR. As a primary standard, 0.1 M NaOH was added to substrate solutions starting at pH 1. The pH changes were recorded and plotted against the volume of added 0.1 M NaOH to obtain titration curves. Then pK_a values were calculated using the Henderson−Hasselbach equation (eq 2), where the pK_a equals the pH at one-half the equivalence point.

$$\mathrm{pH} = \mathrm{p}K_a + \log(A^-/\mathrm{HA}) \quad (2)$$

The pK_a of 9.4 in CoMSH is assigned to the thiol group. This value is lower than that of ethanethiol (10.2), most likely fine tuned by the influence of the sulfonate group. The sulfonate group pK_a of 1.9 in CoMSH and 2.5 in methyl-SCoM is as expected due to the inductive effect of the methyl group (electron donating), which destabilizes the conjugate base, thus increasing the pK_a (Figure S1). The pH titration of HSCoB starting at pH 1.1 yields four pK_a values (Table 2A) that can be attributed to phosphate ionization-1, carboxylate, phosphate ionization-2, and the thiol group (Figure S2).

To distinguish between the carboxylate and phosphate ionization-1, ^{31}P NMR and ^{1}H NMR chemical shift changes with changes in pH were monitored. The pK_a of 9.2 can be unambiguously ssigned to the −SH group of HSCoB (Figure S3; Table 2B). In CoMSSCoB, the pK_a of the sulfonate group could not be determined because it is presumably lower than 1. The pK_a of 1.8 in the case of the heterodisulfide is assigned to the first ionization of phosphate based on the ^{31}P NMR results (Figure S4).

X-ray Absorption Studies. XAS studies, including Ni−K edge, pre-edge, and EXAFS of MCRred1 and MCRred1-silent with and without heterodisulfide substrates CoMSSCoB and CoMSSCoB$_6$, were carried out to establish the changes in coordination around the Ni(I) in the enzyme substrate binding pocket.

Ni(I)−MCRred1 was purified as MCRred1c (CoMSH bound) in the presence of 10 mM CoMSH to stabilize the active enzyme. Subsequently, it was extensively buffer exchanged with 50 mM Tris-HCl, pH 7.6, in an attempt to remove any bound Ni(I)−SCoM and is denoted as MCRred1 in the XAS samples. However, these preparations result in a mixture of Ni(I) and Ni(II). On the basis of the relative UV−vis absorbances of these states, the MCRred1 XAS spectra were corrected for 30% MCRred1c-silent impurity containing a Ni(II)−thiolate from CoM with its sulfonate bound to Arg-γ120 (described above). The Ni(II)−MCRred1-silent sample was prepared by buffer exchange (in 50 mM Tris-HCl, pH 7.6) of an MCRred1c sample, auto-oxidized by prolonged storage in the anaerobic chamber. This MCRred1-silent is hereafter referred to as MCRred1c-silent.

Ni K-edge XAS and EXAFS of MCRred1 show that the Ni(I) is pentacoordinate with 4N (ring) and 1O (axial Gln) (Figure 10 A and Table 3). On the other hand, MCRred1c-silent consists of a hexacoordinate Ni(II) with 4N (ring), 1 O (axial Gln), and a −S ligand from covalently bound CoMSH. The covalent nature of the Ni(II)−S bond prevents the loss of CoMSH during extensive buffer exchange. This is also evident in the EXAFS of MCRred1c-silent, where there is a higher contribution from the Ni−S bond and the data can be assigned to a hexacoordinated Ni(II) (Figure 10A, Table 3)

Addition of substrates CoMSSCoB and CoMSSCoB$_6$ to MCRred1 results in (a) a decrease in the back-bonding contribution at ~8334.5 eV in the Ni-pre edge region (Figure 10 B) and (b) a modest increase in the EXAFS and FT data. FEFF fits suggest the presence of a sixth, weaker, light atom (O/N) ligand to the Ni(I) at ~2.17 Å (Figure 11A and 11B, top). Attempts to fit the data without the weak Ni−O component (Figure 11A and 11 B, bottom) or by increasing the Ni−S coordination led to statistically poorer fits. Thus, the EXAFS

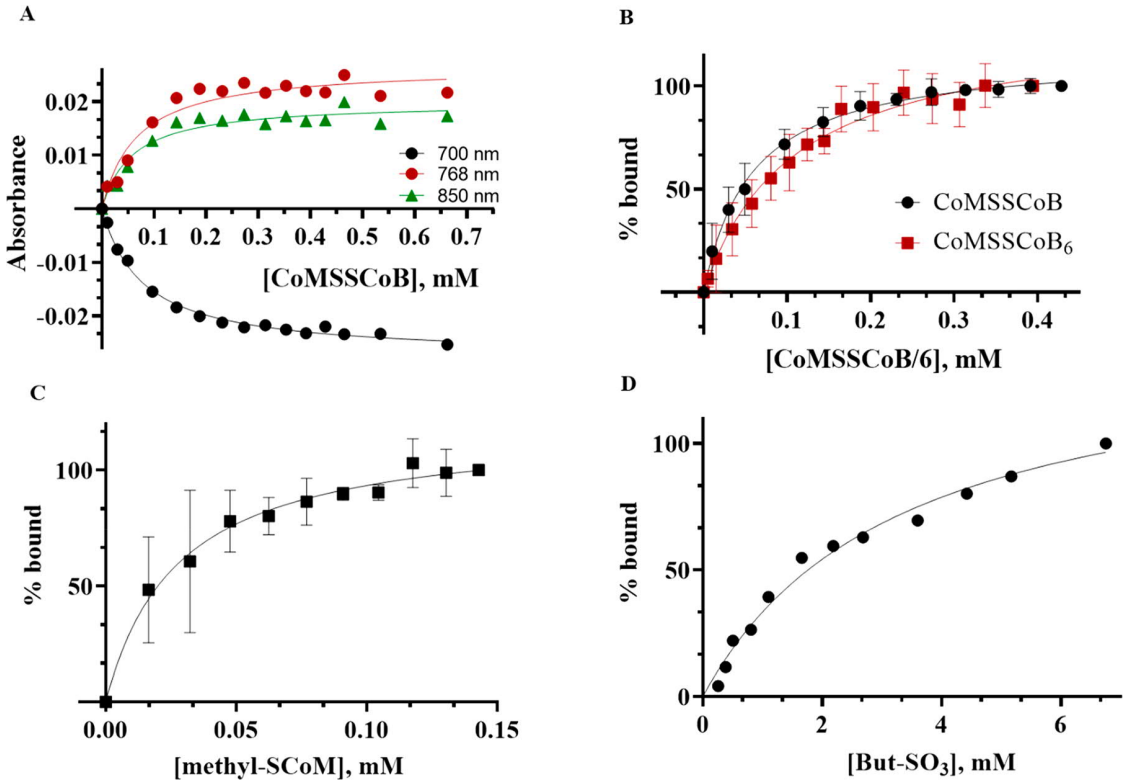

Figure 9. Determination of dissociation constants for MCR substrates and analogs based on NIR spectral changes. (A) Plot of changes in absorbance at 700 (black), 768 (red), and 850 nm (green) with increasing concentrations of CoMSSCoB. (B) Plot of percent of enzyme bound to substrate with addition of increasing concentrations of CoMSSCoB (black) and CoMSSCoB$_6$ (red). Data was fit to a one-site-specific binding equation to obtain K_d values of 57.4 ± 5.4 and 105.3 ± 10.9 μM for CoMSSCoB and CoMSSCoB$_6$, respectively. (C and D) One-site-specific binding isotherms for methyl-SCoM and But-SO$_3$ give K_d values of 27.53 ± 7.6 μM and 3.3 ± 0.6 mM, respectively.

Table 2. pK_a Values of Ionizable Groups of the Substrates As Measured by pH Titrations and NMR

	pH titrations				
substrate	−SO_3H	OPO(OH)(OH)	−COOH	OPO(OH)O−	−SH
CoMSH	1.9				9.4
methyl-SCoM	2.4				
CoMSSCoB		1.8	4.2	7.3	
HSCoB		2.4	4.4		9.1
		^{31}P NMR		^{1}H NMR	
		pK_a	pK_a (g-^{1}H)	pK_a (h-^{1}H)	pK_a (k-^{1}H)
CoMSSCoB	−SO_3H				<1.25
	OPO(OH)(OH)	2.4			
	OPO(OH)O−	6.6	6.2	6.8	
	−COOH		4.3		
HSCoB	OPO(OH)(OH)	4.8			
	OPO(OH)O−	6.6	6.4	7.2	
	−COOH		4.1		

data strongly indicate the formation of a hexacoordinated Ni(I) model for MCRred1 plus CoMSSCoB or CoMSSCoB$_6$. Both heterodisulfide substrates are tethered to the top of the substrate binding channel via phosphate and carboxylate groups with the methylene chain of the CoB moiety making its way into the channel, as described above and shown in Figure 1. The sulfonate group of the CoMS part of the molecule is within bonding distance of the Ni(I) and is likely the sixth ligand. In contrast, addition of the heterodisulfide substrates to MCRred1c-silent shows no changes in the pre-edge or Ni-EXAFS, indicating that the heterodisulfide substrate cannot outcompete covalently bound CoMSH in the Ni(II) active site (Figure S6).

The fits for MCRred1 + CoMSSCoB and CoMSSCoB$_6$ are significantly better and statistically relevant when a sixth lighter N/O ligand is included. A Ni(I)−OSO_3 bond is expected to result in a weak interaction, but the heterodisulfides are constrained in a fixed geometry in the substrate binding pocket with little flexibility. The sulfonate is held in position within binding distance to the Ni(I) with CoMSH.

The absence of an increase in the Ni−S component in the FEFF fits to the EXAFS data clearly shows no additional sulfur

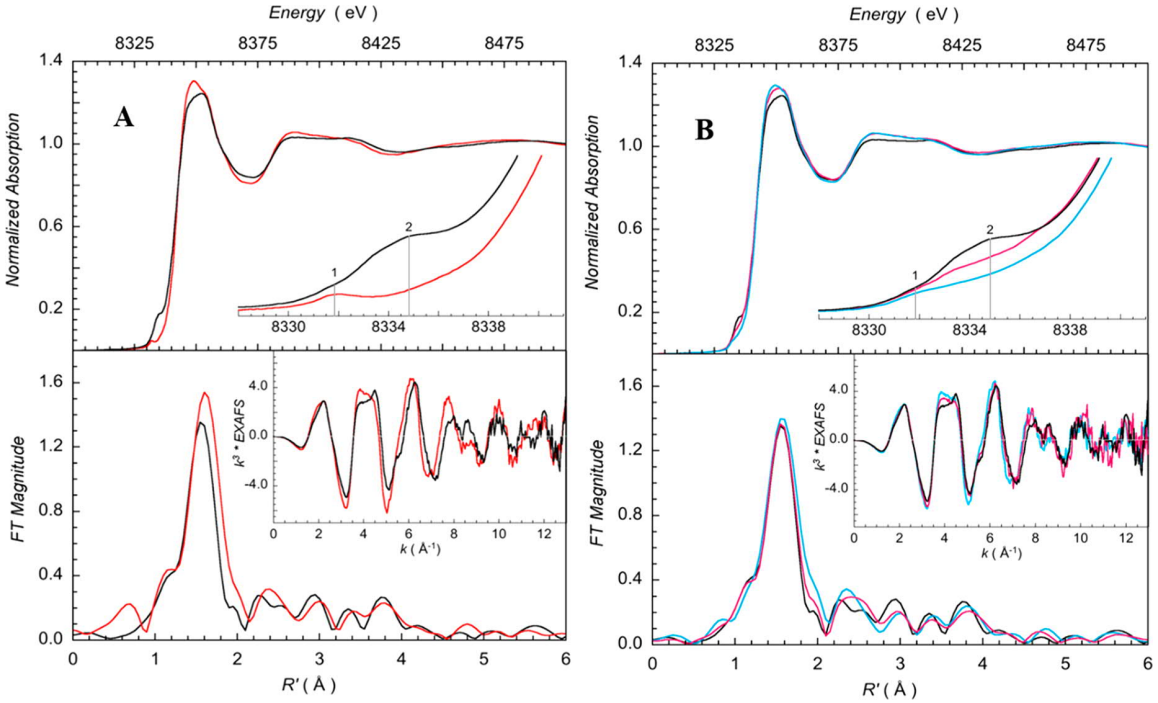

Figure 10. Ni K-edge XAS of MCR + CoMSSCoB. (Top) Comparison of the normalized Ni K-edge XAS data for (A) MCRred1 (black) and MCRred1-silent (red) and (B) MCRred1 (black), MCRred1 + CoMSSCoB (blue) and MCRred1 + CoMSSCoB$_6$ (red). Inset in each plot shows the expanded pre-edge region. Markers at ∼8332 and ∼8334.5 eV represent the 1s → 3d transition and the back-bonding transition involving interactions between the F$_{430}$ ring and the Ni center, respectively. (Bottom) Comparison of the Ni K-edge EXAFS data (inset) and their corresponding Fourier transforms.

Table 3. Bond Distances from XAS

	Ni−N/O (Å, pentacoordinate	Ni−N/O (Å) sixth ligand	Ni−S (Å) sixth ligand from MCRred1-silent
MCRred1	2.03 (4) N ring (1) O Gln		2.39 (0.3) −SHCoM
MCRred1 + CoMSSCoB	2.04 (4) N ring (1) O Gln	2.16 (0.7) −O−SO_2R	2.39 (0.3) −SHCoM
MCRred1 + CoMSSCoB$_6$	2.03 (4) N ring (1) O Gln	2.16 (0.7) −O−SO_2R	2.39 (0.3) −SHCoM
MCRred1c-silent	2.08 (4) N ring 2.20 (1) O Gln		2.42 (1) −SHCoM
MCRred1 + CoMSH + HSCoB (partial formation of MCRred2)	2.05 (4) N ring (1) O Gln	2.18 (0.3)	2.45 (0.7)

atom ligation to Ni(I) on addition of any of the substrates. This is quite significant since all catalytic mechanisms begin with a Ni(I)−thiolate. Thus far, the only experimentally observed Ni(I)−S interaction is with the MCRred2 form, which was generated by addition of HSCoB to MCRred1c. This interaction was previously characterized with pulse EPR and ENDOR studies.[37] Similarly, our EPR spectra of the MCRred2 sample (Figure 12A, bottom) show 40% conversion of MCRred1 to MCRred2 calculated from the relative intensity of g = 2.2098 (rhombic signal from MCRred2) and g = 2.0537 (axial signal from MCRred1) (Table 3).

EPR spectra of the split XAS samples run in parallel show sharpening of the hyperfine signals arising from the ring nitrogens on addition of CoMSSCoB, CoMSSCoB$_6$, methyl-SCoM, and But-SO_3 (Figure 12 B) but not with CoMSH (Figure 12A, middle). The g values (2.2201 and 2.0510) are consistent with previously published EPR data, as summarized.[27] As shown earlier,[38] methyl-SCoM binding results in sharpening of the superhyperfine features. This sharpening is also observed with addition of CoMSSCoB, CoMSSCoB$_6$, and But-SO_3, suggesting that they bind similarly to MCR. To explain this sharpening of the superhyperfine lines, one option is that it results from movement of the Ni(I) into the plane of the F$_{430}$ corphinoid ring due to conversion of a penta- to a hexacoordinate Ni(I) complex. However, the hyperfine splitting values (A_N and A_{Ni}) of MCRred1 and the methyl-SCoM-bound MCRred1m are comparable.[35] Perhaps sharpening of the superhyperfine lines results from a Ni(I)−substrate interaction that reduces the microheterogeneity around the Ni(I) by restricting it to a fixed conformation as the pentacoordinated Ni(I) converts to a hexacoordinated Ni(I) complex with a weak Ni(I)−O−sulfonate interaction. Binding of CoMSH (Figure 12A, middle) does not exhibit the line sharpening observed with the other substrates, consistent with it not forming an axial Ni(I)−O sulfonate complex.

The structural assignments are also consistent with the geometries determined by quantum mechanical calculations of the model systems. A summary of the relevant geometric distances for the three models and the crystal structure 1hbm are summarized in Table 1.

As shown in Figure 5 and Table 1, the Ni−O distance between F$_{430}$ and O-Gln147 is similar in the 3 calculated structures at

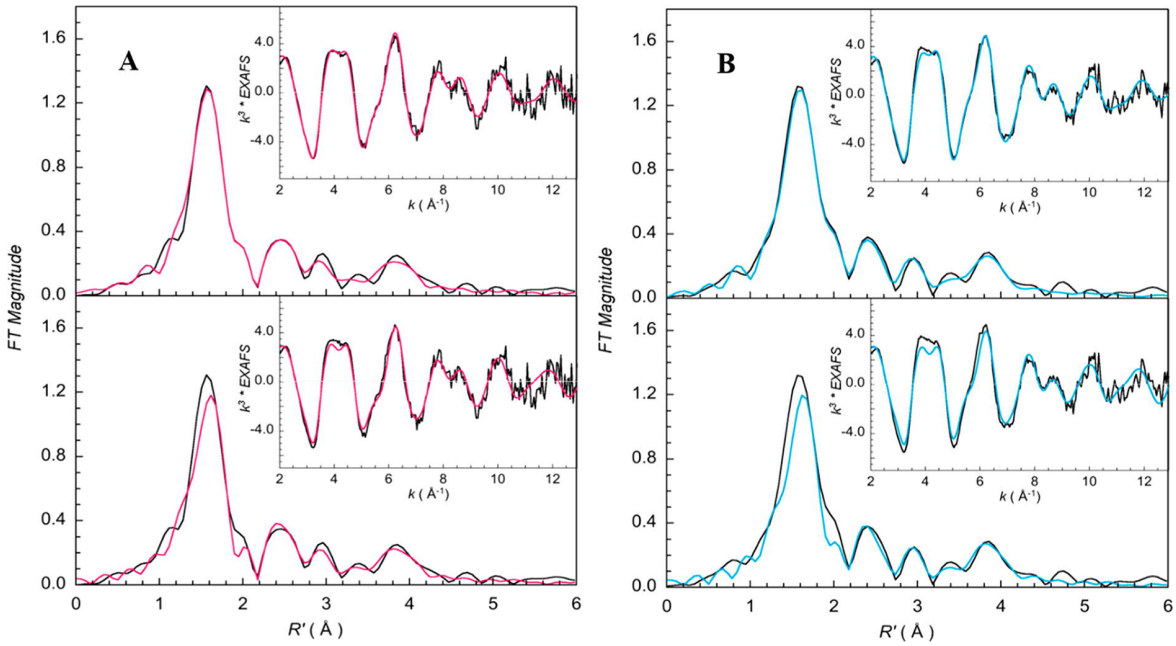

Figure 11. FEFF best-fit Ni K-edge EXAFS data (inset) and corresponding Fourier transforms. Top and bottom figures represent, respectively, fits with and without a longer Ni−O component in the first-shell coordination sphere (see Table 3). (A) MCRred1 + CoMSSCoB$_6$: data (black), fit (red). (B) MCRred1 + CoMSSCoB: data (black), fit (blue).

about 2 Å, whereas the Ni−O between F_{430} and the SO_3^- group varies with a distance of ∼2.4 for models 1 and 2 and is elongated to 2.7 Å in model 3. Similarly, the distances from the Ni to the S atom in the SO_3^- group is ∼0.3 Å longer in model 3, compared to models 1 and 2. In comparison, the crystal structure shows a longer bond between Ni and Gln147 (2.35 Å) but a slightly shorter distance to the nearest oxygen of the SO_3^- group (2.29 Å). The distances between the Ni center and the S_b of HSCoB remain largely unchanged in the three models in Figure 5 and very similar to the crystal structure; however, the Ni−S_m distance varies from ∼6.1 Å in HSCoB-methyl-SCoM to ∼7 Å in CoMSSCoB + CH_4.

Because no crystal structure is available for methyl-SCoM-bound MCRred1, the position of the CH_3 group in methyl-SCoM cannot be verified. However, overlap of the calculated structures of HSCoB-methyl-SCoM (Figure 5, model 2) shows that even in a state where methyl-SCoM would bind to Ni via the SO_3^- group, the CH_3 group can fit in a cavity between the Tyr333, Phe330, and HSCoB, nestled near the thiol group of HSCoB (Figure 5, model 3).

Previous theoretical models that employed a truncated methyl disulfide representation of methyl-SCoM (Figure 6), where the interaction with Ni is considered via the S_m atom, show a Ni−S_m distance of ∼3.7 Å and a much longer Ni−O(Gln147) distance of ∼3.8 Å.[35] Instead, CoMSSCoB (modeled as ethylS−Smethyl) exhibits a Ni−Sm distance of ∼4 Å.

Interestingly, the electronic structure of the Ni center in the present calculations differs from the previous models.[19,35] In these prior models, a single unpaired electron is localized on the Ni center, as characterized by Mulliken spin analysis, resulting in spin ≈ 0.9. The lowest electronic state for the present calculations shows that the overall spin on the Ni center is persistently ∼1.6 with an antiferromagnetically coupled electron delocalized on the carbon atoms in the F_{430} ring, giving an overall state of Ni(I), even though the metal center itself exhibits Ni(II)-like character. The spin assignments for the new structures are reported in Table 4. This unusual electronic state of the Ni may explain the uncommon hexacoordination in the Ni(I).

DISCUSSION

The position of CoMSH in previous crystal structures of the inactive Ni(II) state[27,31] helped prompt the canonical MCR mechanism. Yet, it poses a conundrum for all published MCR catalytic mechanisms. Basically, the question is how can a methyl radical generated from a Ni−thioether interaction with methyl-SCoM at the nickel abstract the H of HSCoB when the reactive sulfurs of the two substrates are 6.4 Å apart? The results described here suggest a solution: methyl-SCoM, the first substrate in the forward reaction, forms a six-coordinate Ni(I)−O complex between a sulfonate oxygen group and the Ni(I) center of F_{430}. Similarly, our work suggests that the first substrate in the reverse reaction, CoMSSCoB, forms a Ni(I)−sulfonate interaction.

While the thiolate of $CoMS^-$ appears to bind tightly to the Ni(II) states of MCR, in the absence of cosubstrate (HSCoB) (Figure 1A), it does not appear to bind to the Ni(I) state. Furthermore, addition of CoMSH to MCRred1 does not alter its Ni(I) NIR or XAS spectra, indicating that MCRred1 is five coordinate, with 4 N from the hydrocorphin ring and an O from Gln-α'147. This assignment is supported by EXAFS data of the Ni(I)−MCRred1m and MCRred1c states.[22] Ni K pre-edge and EXAFS data presented here in addition to time-dependent DFT (TD-DFT) calculations also reinforce the five-coordinate nature of the Ni(I) center when MCRred1 reacts with CoMSH.[29] Furthermore, when MCRred1 is reacted with ^{33}S-substituted Co^{33}SH, no line broadening in the X-band EPR spectrum is observed.[30]

Unlike the neutral effect in the NIR spectra of adding CoMSH to Ni(I)−MCR, addition of methyl-SCoM and the hetero-disulfides CoMSSCoB and CoMSSCoB$_6$ to MCRred1 elicits changes marked in the d−d transitions of the Ni(I) center.

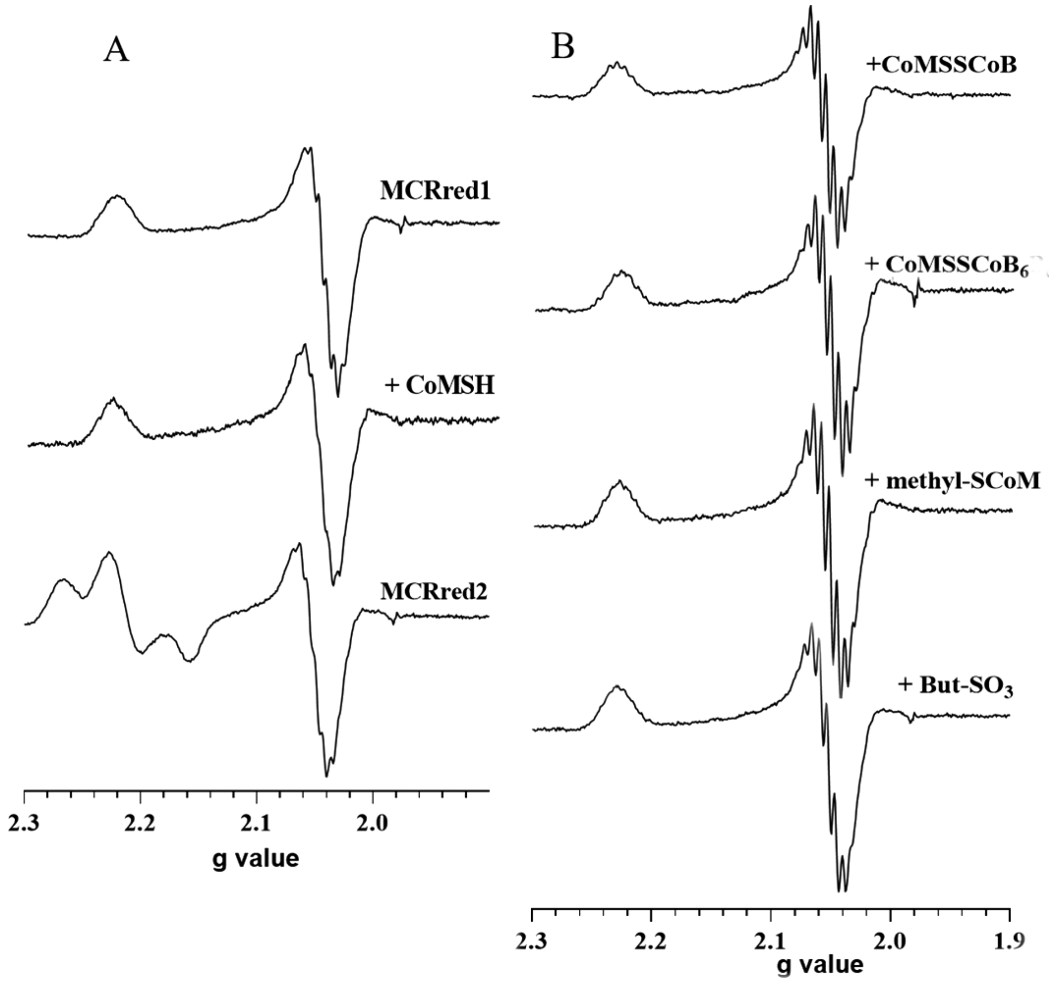

Figure 12. EPR spectra of MCRred1 with substrates (A) MCRred1, MCRred1+ CoMSH, and MCRred2 (MCRred1 + CoMSH + HSCoB) and (B) (top to bottom) MCRred1 + CoMSSCoB, CoMSSCoB$_6$, methyl-SCoM, and But-SO$_3$. Typical Ni(I) EPR signals at 2.2201 and 2.0510 were observed.

Table 4. Electron Spins at Ni and F_{430}

spin[a]	CoMSSCoB + CH_4	HSCoB + methyl-SCoM	methyl-SCoM
Ni	1.6	1.6	1.6
C[a]	−0.56	−0.56	−0.59
C[b]	−0.39	−0.39	−0.35

[a]Calculated using Mulliken population analysis at the Ni and select carbons in F_{430} as shown in Figure 5.

These NIR changes provide accurate K_d values for the Ni(I) complex with these substrates. That substrate mimic butanesulfonate, which lacks the sulfur proposed in the canonical Ni−S interaction, elicits the same NIR changes and convincingly supports our proposal of a Ni(I)−sulfonate complex that initiates catalysis. Our NIR studies are complemented by XAS, quantum mechanical calculations, and TD-DFT studies to characterize the Ni(I) ligand interaction that arises on binding. Furthermore, unlike the computational models described so far, which omitted the sulfonate group of methyl-SCoM using methanethiol as the substrate,[35] we included this in our computations.

On the basis of these studies, we propose an alternate model for methyl-SCoM binding to MCRred1 for the forward reaction (Figure 13) and a new mechanism (Figure 3B) for the catalysis of MCR in the forward and reverse reactions. These suggestions depart from canonical mechanisms, e.g., Figure 3A, which propose a Ni−S (thioether) interaction with methyl-SCoM and a Ni−S (disulfide) interaction with CoMSSCoB. This alternative model mimics the structure of the CoMSSCoB product complex with Ni(II)−MCR and positions the methyl thioether group adjacent to the hydrogen atom of HSCoB, as shown in Figure 5.

Thus, as shown in Figure 5, we propose that the structures of the Ni(I)−methyl-SCoM/HSCoB and the CoMSSCoB complexes mimic that of the X-ray crystal structure of the MCR-silent state in which the heterodisulfide binds with one −O of the sulfonate axially coordinated to the Ni(II) center and makes H-bond contacts with Tyr-α333. The second −O is hydrogen bonded to the lactam ring of the cofactor F_{430} and to the hydroxyl group of Tyr-β367, and the third −O interacts with a water molecule. Similarly, we propose that the CoBS− part of the heterodisulfide substrate makes the same electrostatic and van der Waals contacts as the HSCoB at the top of the channel and along the annular arrangement of the hydrophobic residues along the substrate channel. The −S of the CoB moiety of the heterodisulfide is then placed in the same position as that of HSCoB in the crystal structure.[21]

Thus, in step 1 of both the canonical (Figure 3A) and our proposed (Figure 3B) mechanisms, Ni(I)−MCRred1 (**A**) first binds methyl-CoM and then HSCoB to form the productive

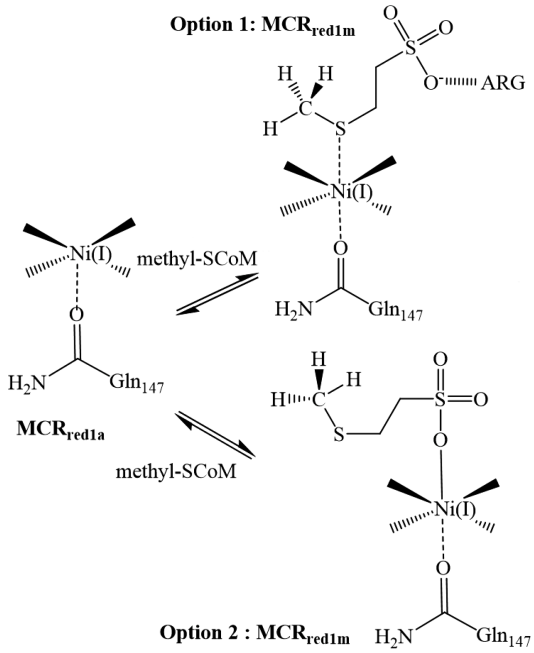

Figure 13. Proposed alternative binding mode for methyl-SCoM to Ni(I)−MCR red1. Option 1 highlights the canonical binding mode through the −S of the thioether. Option 2 is the proposed binding mode through the sulfonate $-O^-$.

ternary complex (**B**).[36] The shaded box(es) in Figure 3A will be addressed below.

In step 2, Ni(I) transfers an electron to methyl-SCoM to promote homolytic cleavage of the C−S bond of methyl-SCoM forming intermediate **C** with the H atom of HSCoB positioned near the CH_3 group of methyl-SCoM. In Figure 3A, the proposed transition state (TS1) for this reaction[35] features a Ni−S (thioether) interaction; however, as described above, prior computational models omitted the sulfonate group of methyl-SCoM; thus, its involvement in the MCR mechanism obviously could not be addressed. In Figure 3B, the methyl-SCoM is flipped 90° with Ni(I)−O (sulfonate) coordination. In both cases, a methyl radical is positioned between the thiolate sulfurs of CoMS− and the H of HSCoB. The mechanistic implication is in the mode of ET—direct Ni → thiolate in Figure 3A and a long distance from the sulfonate to the thioether in Figure 3B.

While there has been active discussion in the biology, chemistry, and physics communities about how it occurs, long-range ET (aka electron tunneling) of 20 Å has been demonstrated in many proteins,[39] such as ribonucleotide reductase.[40,41] Redox equivalents can be transferred even longer distances by multistep tunneling, often called hopping, through intervening amino acid side chains. The well-studied mechanism of proton-coupled ET (called long-range radical transfer) in ribonucleotide reductase[41] is also instructive. Other recent studies discuss the feasibility of ET or PCET over the distances required here.[42−44]

With a maximum velocity of 100 μmol min^{-1} mg^{-1} ($k_{cat} \approx 500$ s^{-1}) for the active MCRred1 state,[45] the time frame for catalysis is on the order of 1−2 ms with a reaction barrier of 15−17 kcal/mol.[19] Since ET from Ni(I) to the S_m of methyl-SCoM does not appear to be rate limiting in the MCR reaction, it would need to also occur in the 1 ms time frame. The required 6.09 Å Ni−Sm distance (Table 1) for coupling the oxidation of Ni(I) to the generation of a methyl radical from methyl-SCoM appears to be compatible with that distance and time frame given that ET is usually not rate limiting in enzymatic redox reactions, like those cited above, and generally occurs over distances of 10−15 Å between redox centers. Metal-initiated radical formation over even longer distances has been observed in various enzyme systems, like those cited above. We hope that our results encourage the evaluation (for instance computationally) of ET transfer rates and mechanisms in MCR to properly address the feasibility of ET or proton-coupled ET in forward and reverse methane synthesis.

In step 3 of methane synthesis, the methyl group abstracts a hydrogen atom from HSCoB to generate methane and a CoBS$^\bullet$ radical (species **D**). Thus far, we have observed only small amounts (~6%) of a radical that we assigned to CoBS$^\bullet$,[46] presumably because unstabilized thiyl radicals are difficult to observe due to their short lifetimes and large spin−orbit coupling with the sulfur atom.[47] Frey and others have used radical clocks and substrate analogs that form stabilized radicals to investigate elusive substrate radicals.[48] The proposed methyl radical, which will likely be even more challenging to visualize, also has not yet been spectroscopically observed.

In step 4 of methane synthesis, the CoBS$^\bullet$ radical reacts with bound CoMSH (through the thiolate, Figure 3A, or sulfonate, Figure 3B) to generate a disulfide anion radical (species **E**), which transfers an electron back to Ni(II) to generate the Ni(I)−CoMSSCoB product (**F**), which we have observed by NIR and XAS spectroscopies. Dissociation of the heterodisulfide in step 5 regenerates the Ni(I) starting state (**A**) for the next round of catalysis.

While our results form a compelling argument for sulfonate binding to the Ni, they do not rule out the possibility that S−Ni binding could occur at some point during or after turnover. For example, as shown in the shaded portion of Figure 3A, while Figure 3B invokes the Ni−sulfonate as the productive complex, an alternative is that the Ni(I)−sulfonate complex undergoes rearrangement to a productive Ni−S(thioether) coordination, as proposed in the canonical mechanism. However, for the reasons discussed above, including that quantitative conversion from species **A** to **B** (or **F** in the reverse reaction) and the kinetic competence of the Ni−sulfonate, we propose the Ni−sulfonate binding mode (Figure 3B) to be the physiologically relevant catalytic species. Thus, we deem rearrangement of the Ni−sulfonate to form the canonical Ni−S binding mode (species **B** to **B′** and **F** to **F′** in Figure 3A) during catalysis to be unlikely.

CONCLUSION

On the basis of our NIR, XAS, and computational studies, we propose an alternate Ni(I)−sulfonate binding mode for methyl-SCoM and CoMSSCoB in methane formation and during reverse methanogenesis, respectively. This proposed binding mode addresses and provides a possible resolution to the difficult recombination of the CoBS$^\bullet$ radical with the Ni−SCoM species over a distance of 6.4 Å to generate the heterodisulfide product. The binding of CoMSSCoB through the sulfonate also provides a viable mechanism of C−H bond activation going in the reverse direction in the situation where the disulfide bond is unable to get closer to the Ni(I) due to the anchoring of the substrate at the top of the channel by electrostatic residues. This revised mechanism obviates the need for substantial active site rearrangements that may involve large thermodynamic and kinetic penalties. This Ni(I)−sulfonate binding provokes the need to reassess the canonical mechanism in favor of one in

which long-range electron transfer (ET) occurs from the F_{430} Ni−corphinoid system to the S atom in the substrates.

METHODS

Organism and Materials. *Methanothermobacter marburgensis* was obtained from the Oregon Collection of Methanogens (Portland, OR) catalog as OCM82.

All buffers, media ingredients, and other reagents were acquired from Sigma. The N_2 (99.98%), CO (99.99%), H_2/CO_2 (80%/20%), and Ultra High Purity (UHP) H_2 (99.999%) gases were obtained from Cryogenic Gases (Grand Rapids, MI).

A stock solution of 83 mM Ti(III) citrate was prepared by adding 0.5 M sodium citrate to Ti(III) trichloride (15% w/v in 2 N hydrochloric acid) under anaerobic conditions and adjusting the pH to 7.0 with 1 M Tris pH 8.0.[49] The concentration of Ti(III) citrate was determined from its UV−vis absorbance at 340 nm (ε = 730 M^{-1} cm^{-1}).

Methyl-SCoM was prepared from CoMSH and methyl iodide.[50] The homodisulfides CoBSSCoB and CoB_6SSCoB_6 were synthesized from their respective 7-bromoheptanoic acid and 6-bromohexanoic acid[51,52] with a change in the final purification step. A RP-PoraPak column was used with an AKTA PURE FPLC system to purify the final homodisulfide with a water/methanol gradient. The heterodisulfide $CoMSSCoB_{/6}$ was synthesized via disulfide exchange between CoMSH and CoBSSCoB or CoB_6SSCoB_6 in anaerobic 400 mM potassium phosphate buffer for 2 h at 45 °C. The reaction was stopped by exposure to oxygen followed by purification on a RP-PoraPak column connected to an AKTA PURE FPLC system. The free thiol form of HSCoB and $HSCoB_6$ was generated by the reduction of the homodisulfide with tris(2-carboxyethyl) phosphine TCEP in an anaerobic chamber, purified using a RP-PoraPak column, and confirmed by HPLC (Phenomenex RP-Fusion C18 column) with a 10 mM potassium phosphate (Buffer A) and acetonitrile (Buffer B) gradient and mass spectrometry

Cell Growth and Purification. Solutions were prepared, and all steps of purification were performed under anaerobic conditions in a Vacuum Atmospheres (Hawthorne, CA) anaerobic chamber maintained under nitrogen gas at an oxygen level below 1 ppm. *M. marburgensis* was cultured on H_2/CO_2 (80/20%) at 65 °C in a 14 L fermenter (New Brunswick Scientific Co., Inc., New Brunswick, NJ) to an optical density of 7−8 at 600 nm in order to increase the yield of MCR-isoenzyme I vs MCR- isoenzyme II. Culture media were prepared as previously described[53] with a slight modification of the sulfur and reducing source by adding 50 mM sodium sulfide (instead of H_2S gas) at a flow rate of 1 mL/min during the entire growth period. The cells were anaerobically harvested, resuspended in 50 mM Tris-HCl, pH 7.6, containing 10 mM CoMSH and 0.1 mM Ti(III) citrate, and transferred into a 1 L serum-stopped anaerobic high-pressure bottle. The headspace of the bottle containing the resuspended cells was purged with CO for 4 h at 30 °C to generate the active MCRred1state as previously described.[54] MCR-I was purified from MCR-II using Q-Sepharose Fast Flow resin packed in a XK 16/20 column compatible with an AKTA PURE FPLC system. The buffer used was 50 mM Tris-HCl and 10 mM CoMSH pH 7.6 (Buffer A) and 50 mM Tris-HCl and 10 mM CoMSH, 1 M NaCl pH 7.6 (Buffer B). Pure MCRred1 was collected in fractions at a gradient centered around 55% Buffer B. The concentration of MCRred1 was determined by UV−vis spectroscopy using extinction coefficients of 27.0 and 9.15 mM^{-1} cm^{-1} at 385 and 420 nm, respectively, using a multiple wavelength calculation as previously described.[53] The concentration of MCRred1-silent, which contains the inactive Ni(II) form of F_{430}, was calculated using extinction coefficients of 22.0 and 12.7 mM^{-1} cm^{-1} at 420 and 385 nm, respectively.[53] This purification method yields between 65% and 75% MCRred1 in the active Ni(I) form and is used as is in all experiments unless otherwise stated.

UV−vis, NIR, and EPR Studies. Absorbance spectra were recorded in the anaerobic chamber using a diode array spectrophotometer HP-8453 instrument. EPR spectra were recorded on a Bruker EMX spectrometer (Bruker Biospin Corp., Billerica, MA) equipped with an Oxford ITC4 temperature controller, a Hewlett-Packard model 5340 automatic frequency counter, and a Bruker gauss meter. The EPR spectroscopic parameters included the following: temperature, 100 K; microwave power, 10 mW; microwave frequency, 9.43 GHz; receiver gain, 2104; modulation amplitude, 10.0 G; modulation frequency, 100 kHz. The spin concentration was determined by double integration of the sample spectrum obtained under nonsaturating conditions and comparison to that of 1 mM copper perchlorate standard. All samples for EPR spectroscopy were prepared in 50 mM Tris-HCl, pH 7.6, in a Vacuum Atmospheres anaerobic chamber.

Determination of Dissociation Constants. The interaction of substrates with MCR was determined by monitoring changes in the near-IR spectrum of active Ni(I) in MCR red1. The enzyme used was prepared by removing CoMSH and Ti(III) citrate from MCR by buffer exchange with 50 mM Tris-HCl, pH 7.6, using Amicon Ultra15 centrifuge filter units with a 30 kDa cutoff (Millipore).

CoMSSCoB, $CoMSSCoB_6$, or methyl-SCoM (0−500 μM) was added in small increments to 50 μM MCR_{red1}, and the changes in the NIR spectra were measured. But-SO_3 or CoMSH (0−10 mM) was added to 50 μM MCRred1−Ni(I) in order to monitor the changes induced due to substrate binding. The changes in absorbance (700, 768, and 850 nm) were plotted against substrate concentration and fit to a one-site-binding isotherm to obtain the dissociation constants for the various substrates. Instantaneous changes in absorbance were recorded in order to study binding, and the titration data was collected over 5 min wherein no redox change with Ni(I) was observed.

XAS. The Ni K-edge XAS studies on MCR were measured at the Stanford Synchrotron Radiation Lightsource (SSRL) on the unfocused 20 pole 2 T wiggler sidestation beamline 7-3 under nonstandard ring conditions of 3 GeV and ∼500 mA (low-alpha operations mode at SSRL). A Si(220) double-crystal monochromator was used for energy selection. The no-M0 mirror configuration was used, and components of higher harmonics were rejected by detuning the monochromator by ∼30%. All samples were measured as solutions, which were transferred to 1 mm Delrin XAS cells with 1 mil Kapton tape windows under anaerobic conditions, immediately frozen after preparation, and stored under liquid N_2. During data collection, samples were maintained at a constant temperature of ∼10 K using a closed-cycle CryoIndustries liquid helium cryocooler. Data were measured to k = 13 $Å^{-1}$ (fluorescence mode) using a Canberra Ge 30-element array detector. Internal energy calibration was accomplished by simultaneous measurement of the absorption of a Ni foil placed between two ionization chambers situated after the sample. The first inflection point of the foil spectrum was fixed at 8331.6 eV. The samples were monitored for photoreduction, and a fresh spot was chosen for data collection after every three scans. However, no visual change in the rising edge energy position or the pre-edge features (associated with the Ni(I) and Ni(II) forms) was observed over successive scans, indicating that all of the samples were resistant to photoreduction under the reduced current experimental conditions. Data presented here have been averaged over 12 scans or more depending on the species. Data were processed by fitting a second-order polynomial to the pre-edge region and subtracting this from the entire spectrum as background. A four-region spline of orders 2, 3, 3, and 3 was used to model the smoothly decaying postedge region. The data were normalized by subtracting the cubic spline and assigning the edge jump to 1.0 at 8335 eV using the Pyspline[55] program. Data were then renormalized in Kaleidagraph for comparison and quantification purposes.

Theoretical EXAFS signals $\chi(k)$ were calculated using FEFF (Macintosh version 8.4).[56−58] The initial structural model for MCR was obtained from the crystal structure and modified in Avogadro to consider O− and S− axial ligands.[59] The input structure was improved based on preliminary EXAFS fit parameters to generate more accurate theoretical EXAFS signals. Data fitting was performed in EXAFSPAK.[60] The structural parameters that varied during the fitting process were the bond distance (R) and the bond variance σ^2, which is related to the Debye−Waller factor resulting from thermal motion and static disorder of the absorbing and scattering atoms. The nonstructural parameter ΔE_0 (E_0 is the energy at which k = 0) was also allowed to vary but was restricted to a common value for every component in a given fit. Coordination numbers were systematically varied in the course of the fit

but were fixed within a given fit. The fits to the MCRred1-silent yielded metrical parameters nearly identical with those reported earlier. The presence of MCRred1-silent in the reduced MCRred1 was accounted for by including a 0.4 coordination number Ni−S path fixed at the distance obtained from the MCRred1-silent fit.

A 140 μL amount of sample of 600 μM MCR red1 [70% Ni(I)] incubated with various substrates CoMSSCoB (20 mM), CoMSSCoB$_6$ (30 mM), methyl-SCoM (10 mM), But-SO$_3$ (40 mM) or CoMSH (40 mM), and MCR red1 [70% Ni(I)] (600 μM) + CoMSH (10 mM) + HSCoB$_7$/HSCoB$_6$ (20 mM) were prepared in 50 mM Tris-HCl pH 7.6 in 40% glycerol anaerobically. A 90 μL of each sample was frozen in a XAS cell, and 50 μL of the same sample added to 100 μL of 50 mM Tris-HCl pH 7.6 was frozen in EPR tubes for measurement.

pK_a Measurements. pK_a measurements of the various substrates were carried out using acid−base titrations with 0.1 M standard sodium hydroxide solution (Sigma) to obtain titration curves. ^{31}P NMR and ^{1}H NMR were measured at various pH values for all of the substrates, and the changes in the chemical shifts with pH were recorded. pK_a values for the various functional groups (carboxylate, phosphate, and thiol) were obtained by plotting chemical shift as a function of pH.

Computational Studies. Quantum mechanical calculations were done using the NWChem program[61] employing thr DFT methodology. All structures were optimized using the B3LYP[62,63] functional, and the dispersion correction was added using Grimme's D3 correction.[64] All nonmetal atoms were represented with the 6-31G* Gaussian basis set,[65] and for the Ni center we used the lanl2dz ECP basis set.[66] The structures were extracted from the crystal structure deposited in the PDB bank under code 1hbm. Points of truncation from the full structure are marked with an asterisk in Figures 5 and 6, where the model is shown. The truncated bonds were terminated with hydrogens. In the geometry optimization procedure, the heavy atoms at the truncated points were fixed in space. The structures were optimized in the gas phase.

The UV−vis spectra were calculated using the TD-DFT[67−69] approach in NWChem using the RPA approximation. The wave functions were optimized at the same level of theory used in the geometry optimization, and a total of 50 excited states were calculated and used in the reconstruction of the spectra using Gaussian broadening functions.

AUTHOR INFORMATION

Corresponding Author

Stephen W. Ragsdale − *Department of Biological Chemistry, University of Michigan Medical School, Ann Arbor, Michigan 48103, United States;* orcid.org/0000-0003-3938-8906; Email: sragsdal@umich.edu

Authors

Anjali Patwardhan − *Department of Biological Chemistry, University of Michigan Medical School, Ann Arbor, Michigan 48103, United States*

Ritimukta Sarangi − *Stanford Synchrotron Radiation Lightsource, SLAC National Accelerator Laboratory, Menlo Park, California 94025, United States;* orcid.org/0000-0002-2764-2279

Bojana Ginovska − *Pacific Northwest National Laboratory, Richland, Washington 99354, United States;* orcid.org/0000-0003-0165-8202

Simone Raugei − *Pacific Northwest National Laboratory, Richland, Washington 99354, United States;* orcid.org/0000-0001-9118-8480

Author Contributions

The manuscript was written through contributions of all authors. All authors have given approval to the final version of the manuscript.

Notes

The authors declare no competing financial interest.

ACKNOWLEDGMENTS

The content is solely the responsibility of the authors and does not necessarily represent the official views of the Department of Energy. We thank Daniel Esckilsen for his help with MCR purification. Work in S.W.R.'s group was supported by the US Department of Energy (DOE), Office of Science, Basic Energy Sciences (BES) (Grant DE-FG02−08ER15931). The SSRL Structural Molecular Biology Program was supported by the DOE Office of Biological and Environmental Research and by the National Institutes of Health, National Institute of General Medical Sciences (P30GM133894). Support for S.R. and B.G. was provided by the DOE, Office of Science, Office of Basic Energy Sciences, Division of Chemical Sciences, Geosciences, and Biosciences and was performed in part using the Molecular Sciences Computing Facility (MSCF) in the Environmental Molecular Sciences Laboratory, a DOE User Facility located at the Pacific Northwest National Laboratory (PNNL). PNNL is operated by Battelle for the DOE under Contract number DE-AC05-75RL01830.

ABBREVIATIONS

AOM, anaerobic oxidation of methane; HSCoB, coenzyme *B*,*N*-7-mercaptoheptanoylthreonine phosphate; HSCoB$_6$, *N*-6-mercaptohexanoylthreonine phosphate; EPR, electron paramagnetic resonance; ENDOR, electron nuclear double resonance; ET, electron transfer; MCD, magnetic circular dichroism; MCR, methyl-CoM reductase; methyl-SCoM, *S*-methyl-2-mercaptoethanesulfonate; But-SO$_3$, butanesulfonate; CoMSH, 2-mercaptoethanesulfonate; CoMSSCoB, heterodisulfide of coenzyme M and coenzyme B; NIR, near-infrared; RR, resonance Raman spectroscopy; TS, transition state; XAS, X-ray absorption spectroscopy; EXAFS, extended X-ray absorption Fourier transform spectroscopy; NMR, nuclear magnetic resonance spectroscopy

REFERENCES

(1) Ankel-Fuchs, D.; Thauer, R. K. Methane formation from methyl-coenzyme M in a system containing methyl-coenzyme M reductase, component B and reduced cobalamin. *Eur. J. Biochem.* **1986**, *156* (1), 171−7.

(2) Shima, S.; Thauer, R. K. Methyl-coenzyme M reductase and the anaerobic oxidation of methane in methanotrophic Archaea. *Curr. Opin. Microbiol.* **2005**, *8* (6), 643−8.

(3) DeLong, E. F. Microbiology - Resolving a methane mystery. *Nature* **2000**, *407*, 577−79.

(4) Blake, D. R.; Rowland, F. S. Continuing worldwide increase in tropospheric methane, 1978−1987. *Science* **1988**, *239*, 1129−1131.

(5) Atreya, S. K.; Mahaffy, P. R.; Wong, A. Methane and related trace species on Mars: Origin, loss, implications for life, and habitability. *Planet. Space Sci.* **2007**, *55*, 358−369.
(6) Thauer, R. K. Biochemistry of methanogenesis: a tribute to Marjory Stephenson. *Microbiology* **1998**, *144*, 2377−2406.
(7) Hintelmann, H. Organomercurials. Their formation and pathways in the environment. *Met Ions Life Sci.* **2010**, *7*, 365−401.
(8) Metcalf, W. W.; Griffin, B. M.; Cicchillo, R. M.; Gao, J.; Janga, S. C.; Cooke, H. A.; Circello, B. T.; Evans, B. S.; Martens-Habbena, W.; Stahl, D. A.; van der Donk, W. A. Synthesis of methylphosphonic acid by marine microbes: a source for methane in the aerobic ocean. *Science* **2012**, *337* (6098), 1104−7.
(9) *Methods in Methane Metabolism, Part A: Methanogenesis*; Elsevier, 2011; Vol. *494*, p 373.
(10) *Methods in Methane Metabolism, Part B: Methanotrophy*; Elsevier, 2011; Vol. *495*, p 360.
(11) Lashoff, D. A.; Ahuja, D. Relative contributions of greenhouse gas emissions to global warming. *Nature* **1990**, *344*, 529−531.
(12) Solomon, S.; Manning, M.; Marquis, M.; Qin, D. AR4 Climate change 2007: The Physical Science Basis. *Contribution of Working Group I to the Fourth Assessment Report of the Intergovernmental Panel on Climate Change, 2007*; Cambridge University Press, 2007; Vol. *4*.
(13) Arndtsen, B. A.; Bergman, R. G.; Mobley, T. A.; Peterson, T. H. Selective intermolecular carbon-hydrogen bond activation by synthetic metal complexes in homogeneous solution. *Acc. Chem. Res.* **1995**, *28* (3), 154−162.
(14) Friedmann, H. C.; Klein, A.; Thauer, R. K. Biochemistry of coenzyme F430, a nickel porphinoid involved in methanogensis. In *Biosynthesis of Tetrapyrroles*, Jordan, P. M., Ed.; Elsevier Science Publishers: Amsterdam, 1991; Chapter 4, pp 139−154.
(15) Diekert, G.; Klee, B.; Thauer, R. K. Nickel, a component of factor F_{430} from *Methanobacterium thermoautotrophicum*. *Arch. Microbiol.* **1980**, *124*, 103−106.
(16) Diekert, G.; Jaenchen, R.; Thauer, R. K. Biosynthetic evidence for a nickel tetrapyrrole structure of factor F_{430} from *Methanobacterium thermoautotrophicum*. *FEBS Lett.* **1980**, *119*, 118−120.
(17) Whitman, W. B.; Wolfe, R. S. Presence of nickel in Factor F430 from *Methanobacterium bryantii*. *Biochem. Biophys. Res. Commun.* **1980**, *92*, 1196−1201.
(18) Chen, S.-L.; Pelmenschikov, V.; Blomberg, M. R. A.; Siegbahn, P. E. M. Is there a Ni-methyl intermediate in the mechanism of methyl-coenzyme M reductase? *J. Am. Chem. Soc.* **2009**, *131* (29), 9912−3.
(19) Wongnate, T.; Sliwa, D.; Ginovska, B.; Smith, D.; Wolf, M. W.; Lehnert, N.; Raugei, S.; Ragsdale, S. W. The radical mechanism of biological methane synthesis by methyl-coenzyme M reductase. *Science* **2016**, *352* (6288), 953−8.
(20) Thauer, R. K. Methyl (alkyl)-coenzyme M reductases: nickel F-430-containing enzymes involved in anaerobic methane formation and in anaerobic oxidation of methane or of short chain alkanes. *Biochemistry* **2019**, *58* (52), 5198−5220.
(21) Ermler, U.; Grabarse, W.; Shima, S.; Goubeaud, M.; Thauer, R. K. Crystal structure of methyl-coenzyme M reductase: the key enzyme of biological methane formation. *Science* **1997**, *278* (5342), 1457−62.
(22) Grabarse, W.; Mahlert, F.; Duin, E. C.; Goubeaud, M.; Shima, S.; Thauer, R. K.; Lamzin, V.; Ermler, U. On the mechanism of biological methane formation: structural evidence for conformational changes in methyl-coenzyme M reductase upon substrate binding. *J. Mol. Biol.* **2001**, *309* (1), 315−30.
(23) Grabarse, W. G.; Mahlert, F.; Shima, S.; Thauer, R. K.; Ermler, U. Comparison of three methyl-coenzyme M reductases from phylogenetically distant organisms: Unusual amino acid modification, conservation and adaptation. *J. Mol. Biol.* **2000**, *303* (2), 329−344.
(24) Cedervall, P. E.; Dey, M.; Li, X.; Sarangi, R.; Hedman, B.; Ragsdale, S. W.; Wilmot, C. M. Structural analysis of a Ni-methyl species in methyl-coenzyme M reductase from Methanothermobacter marburgensis. *J. Am. Chem. Soc.* **2011**, *133* (15), 5626−8.
(25) Cedervall, P. E.; Dey, M.; Pearson, A. R.; Ragsdale, S. W.; Wilmot, C. M. Structural insight into methyl-coenzyme M reductase chemistry using coenzyme B analogues. *Biochemistry* **2010**, *49* (35), 7683−93.
(26) Duin, E. C.; Cosper, N. J.; Mahlert, F.; Thauer, R. K.; Scott, R. A. Coordination and geometry of the nickel atom in active methyl-coenzyme M reductase from Methanothermobacter marburgensis as detected by X-ray absorption spectroscopy. *JBIC, J. Biol. Inorg. Chem.* **2003**, *8* (1−2), 141−8.
(27) Grabarse, W. G.; Mahlert, F.; Duin, E. C.; Goubeaud, M.; Shima, S.; Thauer, R. K.; Lamzin, V.; Ermler, U. On the mechanism of biological methane formation: Structural evidence for conformational changes in methyl-coenzyme M reductase upon substrate binding. *J. Mol. Biol.* **2001**, *309* (1), 315−330.
(28) Tang, Q.; Carrington, P. E.; Horng, Y. C.; Maroney, M. J.; Ragsdale, S. W.; Bocian, D. F. X-ray absorption and resonance Raman studies of methyl-coenzyme M reductase indicating that ligand exchange and macrocycle reduction accompany reductive activation. *J. Am. Chem. Soc.* **2002**, *124* (44), 13242−56.
(29) Sarangi, R.; Dey, M.; Ragsdale, S. W. Geometric and electronic structures of the Ni(I) and methyl-Ni(III) intermediates of methyl-coenzyme M reductase. *Biochemistry* **2009**, *48* (14), 3146−56.
(30) Ebner, S.; Jaun, B.; Goenrich, M.; Thauer, R. K.; Harmer, J. Binding of coenzyme B induces a major conformational change in the active site of methyl-coenzyme M reductase. *J. Am. Chem. Soc.* **2010**, *132* (2), 567−75.
(31) Ermler, U.; Grabarse, W.; Shima, S.; Goubeaud, M.; Thauer, R. K. Crystal structure of methyl-Coenzyme M reductase: the key enzyme of biological methane formation. *Science* **1997**, *278*, 1457−1462.
(32) Hinderberger, D.; Ebner, S.; Mayr, S.; Jaun, B.; Reiher, M.; Goenrich, M.; Thauer, R. K.; Harmer, J. Coordination and binding geometry of methyl-coenzyme M in the red1m state of methyl-coenzyme M reductase. *JBIC, J. Biol. Inorg. Chem.* **2008**, *13* (8), 1275−89.
(33) Lin, C.-Y.; Power, P. P. Complexes of Ni (I): A "rare" oxidation state of growing importance. *Chem. Soc. Rev.* **2017**, *46* (17), 5347−5399.
(34) Arendt, K. M.; Doyle, A. G. Dialkyl Ether Formation by Nickel-Catalyzed Cross-Coupling of Acetals and Aryl Iodides. *Angew. Chem., Int. Ed.* **2015**, *54* (34), 9876−9880.
(35) Chen, S.-L.; Blomberg, M. R. A.; Siegbahn, P. E. M. How Is Methane Formed and Oxidized Reversibly When Catalyzed by Ni-Containing Methyl-Coenzyme M Reductase? *Chem. - Eur. J.* **2012**, *18* (20), 6309−6315.
(36) Wongnate, T.; Ragsdale, S. W. The reaction mechanism of methyl-coenzyme M reductase: how an enzyme enforces strict binding order. *J. Biol. Chem.* **2015**, *290* (15), 9322−34.
(37) Finazzo, C.; Harmer, J.; Jaun, B.; Duin, E. C.; Mahlert, F.; Thauer, R. K.; Van Doorslaer, S.; Schweiger, A. Characterization of the MCRred2 form of methyl-coenzyme M reductase: a pulse EPR and ENDOR study. *JBIC, J. Biol. Inorg. Chem.* **2003**, *8* (5), 586−93.
(38) Mahlert, F.; Grabarse, W.; Kahnt, J.; Thauer, R. K.; Duin, E. C. The nickel enzyme methyl-coenzyme M reductase from methanogenic archaea: in vitro interconversions among the EPR detectable MCR-red1 and MCR-red2 states. *JBIC, J. Biol. Inorg. Chem.* **2002**, *7* (1−2), 101−12.
(39) Gray, H. B.; Winkler, J. R. Electron Flow through Proteins. *Chem. Phys. Lett.* **2009**, *483* (1−3), 1−9.
(40) Reece, S. Y.; Seyedsayamdost, M. R. Long-range proton-coupled electron transfer in the Escherichia coli class Ia ribonucleotide reductase. *Essays Biochem.* **2017**, *61* (2), 281−292.
(41) Minnihan, E. C.; Nocera, D. G.; Stubbe, J. Reversible, long-range radical transfer in E. coli class Ia ribonucleotide reductase. *Acc. Chem. Res.* **2013**, *46* (11), 2524−35.
(42) Lampret, O.; Duan, J.; Hofmann, E.; Winkler, M.; Armstrong, F. A.; Happe, T. The roles of long-range proton-coupled electron transfer in the directionality and efficiency of [FeFe]-hydrogenases. *Proc. Natl. Acad. Sci. U. S. A.* **2020**, *117* (34), 20520−20529.
(43) Teo, R. D.; Rousseau, B. J.; Smithwick, E. R.; Di Felice, R.; Beratan, D. N.; Migliore, A. Charge transfer between [4Fe4S] proteins

and DNA is unidirectional: Implications for biomolecular signaling. *Chem.* **2019**, *5* (1), 122−137.
(44) Teo, R. D.; Wang, R.; Smithwick, E. R.; Migliore, A.; Therien, M. J.; Beratan, D. N. Mapping hole hopping escape routes in proteins. *Proc. Natl. Acad. Sci. U. S. A.* **2019**, *116* (32), 15811−15816.
(45) Goubeaud, M.; Schreiner, G.; Thauer, R. K. Purified methyl-coenzyme-M reductase is activated when the enzyme-bound coenzyme F_{430} is reduced to the nickel(I) oxidation state by titanium(III) citrate. *Eur. J. Biochem.* **1997**, *243* (1−2), 110−114.
(46) Dey, M.; Li, X.; Kunz, R. C.; Ragsdale, S. W. Detection of organometallic and radical intermediates in the catalytic mechanism of methyl-coenzyme M reductase using the natural substrate methyl-coenzyme M and a coenzyme B substrate analogue. *Biochemistry* **2010**, *49* (51), 10902−11.
(47) Symons, M. C. R. On the electron spin resonance detection of RS radicals in irradiated solids: radicals of type $RSSR^-$, $RS{-}SR_2$, and $R_2SSR_2^+$. *J. Chem. Soc., Perkin Trans. 2* **1974**, *2*, 1618−1620.
(48) Frey, P. A. Radicals in enzymatic reactions. *Curr. Opin. Chem. Biol.* **1997**, *1* (3), 347−356.
(49) Zehnder, A. J. B.; Wuhrmann, K. Titanium(Iii) Citrate as a Nontoxic Oxidation-Reduction Buffering System for Culture of Obligate Anaerobes. *Science* **1976**, *194* (4270), 1165−1166.
(50) Gunsalus, R. P.; Romesser, J. A.; Wolfe, R. S. Preparation of coenzyme M analogues and their activity in the methyl coenzyme M reductase system of Methanobacterium thermoautotrophicum. *Biochemistry* **1978**, *17* (12), 2374−7.
(51) Bobik, T. A.; Wolfe, R. S. Physiological importance of the heterodisulfide of coenzyme M and 7-mercaptoheptanoylthreonine phosphate in the reduction of carbon dioxide to methane in Methanobacterium. *Proc. Natl. Acad. Sci. U. S. A.* **1988**, *85* (1), 60−3.
(52) Noll, K. M.; Donnelly, M. I.; Wolfe, R. S. Synthesis of 7-Mercaptoheptanoylthreonine Phosphate and Its Activity in the Methylcoenzyme-M Methylreductase System. *J. Biol. Chem.* **1987**, *262* (2), 513−515.
(53) Kunz, R. C.; Horng, Y. C.; Ragsdale, S. W. Spectroscopic and kinetic studies of the reaction of bromopropanesulfonate with methyl-coenzyme M reductase. *J. Biol. Chem.* **2006**, *281* (45), 34663−76.
(54) Becker, D. F.; Ragsdale, S. W. Activation of methyl-SCoM reductase to high specific activity after treatment of whole cells with sodium sulfide. *Biochemistry* **1998**, *37* (8), 2639−47.
(55) Tenderholt, A.; Hedman, B.; Hodgson, K. O. In *PySpline: A Modern, Cross-Platform Program for the Processing of Raw Averaged XAS Edge and EXAFS Data, X-ray Absorption Fine Structure - XAFS13*; Hedman, B., Pianetta, P., Eds.; American Institute of Physics, Stanford University, 2007; pp 105−107..
(56) Mustre de Leon, J.; Rehr, J. J.; Zabinsky, S. I.; Albers, R. C. Ab initio curved-wave x-ray-absorption fine structure. *Phys. Rev. B: Condens. Matter Mater. Phys.* **1991**, *44* (9), 4146−4156.
(57) Rehr, J. J.; Mustre de Leon, J.; Zabinsky, S. I.; Albers, R. C. Theoretical X-Ray Absorption Fine-Structure Standards. *J. Am. Chem. Soc.* **1991**, *113* (14), 5135−5140.
(58) Zabinsky, S. I.; Rehr, J. J.; Ankudinov, A.; Albers, R. C.; Eller, M. J. Multiple-Scattering Calculations of X-Ray-Absorption Spectra. *Phys. Rev. B: Condens. Matter Mater. Phys.* **1995**, *52* (4), 2995−3009.
(59) Avogadro: an open-source molecular builder and visualization tool; http://avogadro.openmolecules.net/ (accessed 2012-03-12).
(60) George, G. N. *EXAFSPAK and EDG-FIT*; Stanford Synchrotron Radiation Laboratory, Stanford Linear Accelerator Center: Stanford, CA, 2000.
(61) Aprà, E.; Bylaska, E. J.; de Jong, W. A.; Govind, N.; Kowalski, K.; Straatsma, T. P.; Valiev, M.; van Dam, H. J. J.; Alexeev, Y.; Anchell, J.; Anisimov, V.; Aquino, F. W.; Atta-Fynn, R.; Autschbach, J.; Bauman, N. P.; Becca, J. C.; Bernholdt, D. E.; Bhaskaran-Nair, K.; Bogatko, S.; Borowski, P.; Boschen, J.; Brabec, J.; Bruner, A.; Cauët, E.; Chen, Y.; Chuev, G. N.; Cramer, C. J.; Daily, J.; Deegan, M. J. O.; Dunning, T. H.; Dupuis, M.; Dyall, K. G.; Fann, G. I.; Fischer, S. A.; Fonari, A.; Früchtl, H.; Gagliardi, L.; Garza, J.; Gawande, N.; Ghosh, S.; Glaesemann, K.; Götz, A. W.; Hammond, J.; Helms, V.; Hermes, E. D.; Hirao, K.; Hirata, S.; Jacquelin, M.; Jensen, L.; Johnson, B. G.; Jónsson, H.; Kendall, R. A.; Klemm, M.; Kobayashi, R.; Konkov, V.; Krishnamoorthy, S.; Krishnan, M.; Lin, Z.; Lins, R. D.; Littlefield, R. J.; Logsdail, A. J.; Lopata, K.; Ma, W.; Marenich, A. V.; Martin del Campo, J.; Mejia-Rodriguez, D.; Moore, J. E.; Mullin, J. M.; Nakajima, T.; Nascimento, D. R.; Nichols, J. A.; Nichols, P. J.; Nieplocha, J.; Otero-de-la-Roza, A.; Palmer, B.; Panyala, A.; Pirojsirikul, T.; Peng, B.; Peverati, R.; Pittner, J.; Pollack, L.; Richard, R. M.; Sadayappan, P.; Schatz, G. C.; Shelton, W. A.; Silverstein, D. W.; Smith, D. M. A.; Soares, T. A.; Song, D.; Swart, M.; Taylor, H. L.; Thomas, G. S.; Tipparaju, V.; Truhlar, D. G.; Tsemekhman, K.; Van Voorhis, T.; Vázquez-Mayagoitia, Á.; Verma, P.; Villa, O.; Vishnu, A.; Vogiatzis, K. D.; Wang, D.; Weare, J. H.; Williamson, M. J.; Windus, T. L.; Woliński, K.; Wong, A. T.; Wu, Q.; Yang, C.; Yu, Q.; Zacharias, M.; Zhang, Z.; Zhao, Y.; Harrison, R. J. NWChem: Past, present, and future. *J. Chem. Phys.* **2020**, *152* (18), 184102.
(62) Becke, A. D. Density-Functional Thermochemistry 0.3. The Role of Exact Exchange. *J. Chem. Phys.* **1993**, *98* (7), 5648−5652.
(63) Stephens, P. J.; Devlin, F. J.; Chabalowski, C. F.; Frisch, M. J. Ab-Initio Calculation of Vibrational Absorption and Circular-Dichroism Spectra Using Density-Functional Force-Fields. *J. Phys. Chem.* **1994**, *98* (45), 11623−11627.
(64) Grimme, S.; Antony, J.; Ehrlich, S.; Krieg, H. A consistent and accurate ab initio parametrization of density functional dispersion correction (DFT-D) for the 94 elements H-Pu. *J. Chem. Phys.* **2010**, *132* (15), 154104.
(65) Frisch, M. J.; Pople, J. A.; Binkley, J. S. Self-consistent molecular orbital methods 25. Supplementary functions for Gaussian basis sets. *J. Chem. Phys.* **1984**, *80* (7), 3265−3269.
(66) Hay, P. J.; Wadt, W. R. Ab initio effective core potentials for molecular calculations. Potentials for the transition metal atoms Sc to Hg. *J. Chem. Phys.* **1985**, *82* (1), 270−283.
(67) Bauernschmitt, R.; Haser, M.; Treutler, O.; Ahlrichs, R. Calculation of excitation energies within time-dependent density functional theory using auxiliary basis set expansions. *Chem. Phys. Lett.* **1997**, *264* (6), 573−578.
(68) Jamorski, C.; Casida, M. E.; Salahub, D. R. Dynamic polarizabilities and excitation spectra from a molecular implementation of time-dependent density-functional response theory: N-2 as a case study. *J. Chem. Phys.* **1996**, *104* (13), 5134−5147.
(69) Bauernschmitt, R.; Ahlrichs, R. Treatment of electronic excitations within the adiabatic approximation of time dependent density functional theory. *Chem. Phys. Lett.* **1996**, *256* (4−5), 454−464.